[5] Iwasa Y *et al* 1994 New phases of C_{60} synthesized at high pressure *Science* **264** 1570
[6] Miyazawa K, Satsuki H, Kuwabara M and Akaishi M 2001 Microstructural analysis of high-pressure compressed C_{60} *J. Mater. Res.* **16** 1960–6
[7] Minato J, Miyazawa K, Suga T, Kanda H, Akaishi M, Yamaura K, Muromachi E and Kakisawa H 2005 Characterization of high-pressure sintered C_{60} nanowhiskers and C_{60} powder *J. Mater. Res.* **20** 742–6
[8] Miyazawa K, Akaishi M, Kuwasaki Y and Suga T 2003 Characterizing high-pressure compressed C_{60} whiskers and C_{60} powder *J. Mater. Res.* **18** 166–72
[9] Nakaya M, Nakayama T and Aono M 2004 Fabrication and electron-beam-induced polymerization of C_{60} nanoribbon *Thin Solid Films* **464–5** 327–30
[10] Miyazawa K, Minato J, Fujino M and Suga T 2006 Structural investigation of heat-treated fullerene nanotubes and nanowhiskers *Diam. Relat. Mater.* **15** 1143–6
[11] Popov M, Mordkovich V, Perfilov S, Kirichenko A, Kulnitskiy B, Perezhogin I and Blank V 2014 Synthesis of ultrahard fullerite with a catalytic 3D polymerization reaction of C_{60} *Carbon* **76** 250–6
[12] Blank V, Popov M, Pivovarov G, Lvova N, Gogolinsky K and Reshetov V 1998 Ultrahard and superhard phases of fullerite C_{60}: comparison with diamond on hardness and wear *Diam. Relat. Mater.* **7** 427–31
[13] Miyazawa K, Obayashi A and Kuwabara M 2001 C_{60} nanowhiskers in a mixture of lead zirconate titanate sol–C_{60} toluene solution *J. Am. Ceram. Soc.* **84** 3037–9
[14] Rauwerdink K, Liu J, Kintigh J and Miller G P 2007 Thermal, sonochemical, and mechanical behaviors of single crystal [60] fullerene nanotubes *Microsc. Res. Tech.* **70** 513–21
[15] Miyazawa K and Kuwabara M 2005 Fine carbon wires and methods for producing the same *US Patent* 6890505B2
[16] Miyazawa K 2009 Synthesis and properties of fullerene nanowhiskers and fullerene nanotubes *J. Nanosci. Nanotechnol.* **9** 41–50
[17] Miyazawa K (ed) 2011 *Fullerene Nanowhiskers* (Singapore: Pan Stanford Publishing Pte. Ltd)
[18] Wakahara T, Nemoto Y, Xu M, Miyazawa K and Fujita D 2010 Preparation of endohedral metallofullerene nanowhiskers and nanosheets *Carbon* **48** 3359–63
[19] Miyazawa K, Minato J, Mashino T, Nakamura S, Fujino M and Suga T 2006 Structural characterization of room-temperature synthesized fullerene nanowhiskers *Nukleonika* **51** (Suppl. 1) S41–8
[20] Miyazawa K, Mashino T and Suga T 2004 Liquid phase synthesis of the nanowhiskers of fullerene derivatives *Trans. Mater. Res. Soc. Japan* **29** 537–40
[21] Miyazawa K, Mashino T and Suga T 2003 Structural characterization of the $C_{60}[C(COOC_2H_5)_2]$ whiskers prepared by the liquid–liquid interfacial precipitation method *J. Mater. Res.* **18** 2730–5
[22] Miyazawa K and Suga T 2004 Transmission electron microscopy investigation of fullerene nanowhiskers and needle-like precipitates formed by using C_{60} and (η^2-C_{60})Pt $(PPh_3)_2$ *J. Mater. Res.* **19** 2410–4
[23] Miyazawa K, Minato J, Yoshii T, Fujino M and Suga T 2005 Structural characterization of the fullerene nanotubes prepared by the liquid–liquid interfacial precipitation method *J. Mater. Res.* **20** 688–95
[24] Miyazawa K and Ringor C 2008 Platinum chloride deposition into C_{60} nanotubes *Mater. Lett.* **62** 410–3
[25] Kizuka T, Miyazawa K and Tokumine T 2012 Young's modulus of single-crystal fullerene C_{70} nanotubes *J. Nanotechnol.* **2012** 969357
[26] Liu H *et al* 2002 Imaging as-grown [60] fullerene nanotubes by template technique *J. Am. Chem. Soc.* **124** 13370–1
[27] Zhang X, Qu Y, Piao G, Zhao J and Jiao K 2010 Reduced working electrode based on fullerene C_{60} nanotubes@DNA: characterization and application *Mater. Sci. Eng.* B **175** 159–63
[28] Kizuka T, Miyazawa K and Tokumine T 2012 Synthesis of oriented bundle fibers of fullerene C_{70} crystal nanotubes *J. Nanosci. Nanotechnol.* **12** 2825–8
[29] Miyazawa K, Fujino M, Minato J, Yoshii T, Kizuka T and Suga T 2004 Structure and properties of fullerene nanowhiskers prepared by the liquid–liquid interfacial precipitation method *Proc. SPIE* **5648** 224
[30] Miyazawa K, Kuwasaki Y, Obayashi A and Kuwabara M 2002 C_{60} nanowhiskers formed by the liquid–liquid interfacial precipitation method *J. Mater. Res.* **17** 83–8
[31] Osonoe K, Kano R, Miyazawa K and Tachibana M 2014 Synthesis of C_{70} two-dimensional nanosheets by liquid–liquid interfacial precipitation method *J. Cryst. Growth* **401** 458- 461
[32] Wakahara T, Sathish M, Miyazawa K, Hu C, Tateyama Y, Nemoto Y, Sasaki T and Ito O 2009 Preparation and optical properties of fullerene/ferrocene hybrid hexagonal nanosheets and large-scale production of fullerene hexagonal nanosheets *J. Am. Chem. Soc.* **131** 9940–4
[33] Shrestha L K, Sathish M, Hill J P, Miyazawa K, Tsuruoka T, Sanchez-Ballester N M, Honma I, Ji Q and Ariga K 2013 Alcohol-induced decomposition of Olmstead's crystalline Ag(I)-fullerene heteronanostructure yields'bucky cubes' *J. Mater. Chem.* C **1** 1174–81
[34] Shrestha L K, Hill J P, Tsuruoka T, Miyazawa K and Ariga K 2013 Surfactant-assisted assembly of fullerene (C_{60}) nanorods and nanotubes formed at a liquid–liquid interface *Langmuir* **29** 7195–202
[35] Shrestha L K, Ji Q, Mori T, Miyazawa K, Yamauchi Y, Hill J P and Ariga K 2013 Fullerene nanoarchitectonics: from zero to higher dimensions *Chem. Asian J.* **8** 1662–79
[36] Shrestha L K, Yamauchi Y, Hill J P, Miyazawa K and Ariga K 2013 Fullerene crystals with bimodal pore architectures consisting of macropores and mesopores *J. Am. Chem. Soc.* **135** 586–9
[37] Shrestha L K, Hill J P, Miyazawa K and Ariga K 2012 Mixing antisolvents induced modulation in the morphology of crystalline C_{60} *J. Nanosci. Nanotechnol.* **12** 6380–4
[38] Sathish M and Miyazawa K 2007 Size-tunable hexagonal fullerene (C_{60}) nanosheets at liquid–liquid interface *J. Am. Chem. Soc.* **129** 13816–7
[39] Miyazawa K and Hotta K 2010 The effect of solvent ratio and water on the growth of C_{60} nanowhiskers *J. Cryst. Growth* **312** 2764–70
[40] Cha S I, Miyazawa K and Kim J-D 2008 Vertically well-aligned C_{60} micro-tube crystal array prepared using solution-based one step process *Chem. Mater.* **20** 1667–9
[41] Miyazawa K, Minato J, Mashino T, Yoshii T, Kizuka T, Kato R, Tachibana M and Suga T 2005 Characterization of the liquid-phase synthesized fullerene nanotubes and nanowhiskers *Proc. of the 2nd JSME/ASME Int. Conf. on Materials and Processing 2005—M&P2005: The 13th JSME Materials and Processing Conf. (Seattle, WA, 19–22 June)* pp (SMS23)-1–4
[42] Miyazawa K, Kuriyama R, Shimomura S, Wakahara T and Tachibana M 2014 Growth and FIB-SEM analyses of C_{60} microtubes vertically synthesized on porous alumina membranes *J. Cryst. Growth* **388** 5–11
[43] Cha S I, Miyazawa K and Kim J 2014 Substrate having fullerene thin wires and method for manufacture thereof *United States Patent* 8685160B2
[44] Amer M S, Todd T K and Busbee J D 2011 Effect of linear alcohol molecular size on the self-assembly of fullerene whiskers *Mater. Chem. Phys.* **130** 90–4

[45] Hotta K and Miyazawa K 2008 Growth rate measurement of C_{60} fullerene nanowhiskers *Nano* **3** 355–9
[46] Asaka K, Kato R, Yoshizaki R, Miyazawa K and Kizuka T 2007 Fracture surface and correlation of buckling force with aspect ratio of C_{60} crystalline whiskers *Diam. Relat. Mater.* **16** 1936–9
[47] Kizuka T, Saito K and Miyazawa K 2008 Young's modulus of crystalline C_{60} nanotubes studied by *in situ* transmission electron microscopy *Diam. Relat. Mater.* **17** 972–4
[48] Saito K, Miyazawa K and Kizuka T 2009 Bending process and Young's modulus of fullerene C_{60} nanowhiskers *Japan. J. Appl. Phys.* **48** 010217
[49] Asaka K, Kato R, Miyazawa K and Kizuka T 2006 Buckling of C_{60} whiskers *Appl. Phys. Lett.* **89** 071912
[50] Kato R and Miyazawa K 2011 Cross-sectional structural analysis of C_{60} nanowhiskers by transmission electron microscopy *Diam. Relat. Mater.* **20** 299–303
[51] Kizuka T, Miyazawa K and Tokumine T 2012 Solvation-assisted Young's modulus control of single-crystal fullerene C_{70} nanowhiskers *J. Nanotechnol.* **2012** 583817
[52] Miyazawa K, Hamamoto K, Nagata S and Suga T 2003 Structural investigation of the C_{60}/C_{70} whiskers fabricated by forming liquid–liquid interfaces of toluene with dissolved C_{60}/C_{70} and isopropyl alcohol *J. Mater. Res.* **18** 1096–103
[53] Minato J, Miyazawa K and Suga T 2005 Morphology of C_{60} nanotubes fabricated by the liquid–liquid interfacial precipitation method *Sci. Technol. Adv. Mater.* **6** 272–7
[54] Ji H-X, Hu J-S, Tang Q-X, Song W-G, Wang C-R, Hu W-P, Wan L-J and Lee S-T 2007 Controllable preparation of submicrometer single-crystal C_{60} rods and tubes through concentration depletion at the surfaces of seeds *J. Phys. Chem.* C **111** 10498–502
[55] Ringor C L and Miyazawa K 2009 Fabrication of solution grown C_{60} fullerene nanotubes with tunable diameter *J. Nanosci. Nanotechnol.* **9** 6560–4
[56] Hotta K and Miyazawa K 2008 Growth rate measurement of C_{60} fullerene nanowhiskers *Nano* **3** 355–9
[57] Tachibana M, Kobayashi K, Uchida T, Kojima K, Tanimura M and Miyazawa K 2003 Photo-assisted growth and polymerization of C_{60} 'nano' whiskers *Chem. Phys. Lett.* **374** 279–85
[58] Kobayashi K, Tachibana M and Kojima K 2005 Photo-assisted growth of C_{60} nanowhiskers from solution *J. Cryst. Growth* **274** 617–21
[59] Miyazawa K and Hotta K 2011 The effect of water on the stability of C_{60} fullerene nanowhiskers *J. Nanopart. Res.* **13** 5739–47
[60] Wei M, Luo H, Li N, Zhang S and Gan L 2002 Study of electrochemical properties of pyrrolidinofullerenes by microelectrode voltammetry *Microchem. J.* **72** 115–112
[61] Wakahara T, Miyazawa K, Nemoto Y and Ito O 2011 Diameter controlled growth of fullerene nanowhiskers and their optical properties *Carbon* **49** 4644–9
[62] Miyazawa K, Hirata C and Wakahara T 2014 Influence of the solution volume on the growth of C_{60} nanowhiskers *J. Cryst. Growth* **405** 68–72
[63] Kawasaki S and Sakai E 1967 Measurement of diffusion of gold in copper by elastic scattering of deuteron *J. Nucl. Sci. Technol.* **4** 273–7
[64] Ogawa K, Kato T, Ikegami A, Tsuji H, Aoki N and Ochiai Y 2006 Electrical properties of field-effect transistors based on C_{60} nanowhiskers *Appl. Phys. Lett.* **88** 112109
[65] Somani P R, Somani S P and Umeno M 2007 Toward organic thick film solar cells: three dimensional bulk heterojunction organic thick film solar cell using fullerene single crystal nanorods *Appl. Phys. Lett.* **91** 173503
[66] Shrestha R G, Shrestha L K, Khan A H, Kumar G S, Acharya S and Ariga K 2014 Demonstration of ultrarapid interfacial formation of 1D fullerene nanorods with photovoltaic properties *Appl. Mater. Interfaces* **6** 15597–603
[67] Cho B H, Lee K B, Miyazawa K and Ko W B 2013 Preparation of fullerene (C_{60}) nanowhisker-ZnO nanocomposites by heat treatment and photocatalytic degradation of methylene blue *Asian J. Chem.* **25** 8027–30
[68] Yang J, Lim H, Choi H C and Shin H S 2010 Wavelength-selective silencing of photocurrent in Au-coated C60 wire hybrid *Chem. Commun.* **46** 2575–7
[69] Li H, Tee B C-K, Cha J J, Cui Y, Chung J W, Lee S Y and Bao Z 2012 High-mobility field-effect transistors from large-area solution-grown aligned C_{60} single crystals *J. Am. Chem. Soc.* **134** 2760–5
[70] Miyazawa K, Kuwasaki Y, Hamamoto K, Nagata S, Obayashi A and Kuwabara M 2003 Structural characterization of the C_{60} nanowhiskers formed by the liquid–liquid interfacial precipitation method *Surf. Interface Anal.* **35** 117–20
[71] Larsson M P, Kjelstrup-Hansen J and Lucyszyn S 2007 Dc characterisation of C_{60} whiskers and nanowhiskers *ECS Trans.* **2** 27–38
[72] Xu M S, Pathak Y, Fujita D, Ringor C and Miyazawa K 2008 Covered conduction of individual C_{60} nanowhiskers *Nanotechnology* **19** 075712
[73] Ji H-X, Hu J-S, Wan L-J, Tang Q-X and Hu W-P 2008 Controllable crystalline structure of fullerene nanorods and transport properties of an individual nanorod *J. Mater. Chem.* **18** 328–32
[74] Hannay N B, Geballe T H, Matthias B T, Andres K, Schmidt P and MacNair D 1965 Superconductivity in graphitic compounds *Phys. Rev. Lett.* **14** 225–6
[75] Koike Y, Suematsu H, Higuchi K and Tanuma S 1980 Superconductivity in graphite–alkali metal intercalation compounds *Physica* B **99** 503–8
[76] Weller T E, Ellerby M, Saxena S S, Smith R P and Skipper N T 2005 Superconductivity in the intercalated graphite compounds C_6Yb and C_6Ca *Nat. Phys.* **1** 39–41
[77] Kato R, Miyazawa K, Nishimura T and Wang Z M 2009 High-resolution transmission electron microscopy of heat-treated C_{60} nanotubes *J. Phys.: Conf. Ser.* **159** 012024
[78] Asaka K, Nakayama T, Miyazawa K and Saito Y 2012 Study on structure of heat-treated fullerene nanowhiskers and their field electron emission characteristics *Surf. Interface Anal.* **44** 780–3
[79] Asaka K, Nakayama T, Miyazawa K and Saito Y 2012 Structures and field emission properties of heat-treated C_{60} fullerene nanowhiskers *Carbon* **50** 1209–15
[80] Ekimov E A, Sidorov V A, Bauer E D, Mel'nik N N, Curro N J, Thompson J D and Stishov S M 2004 Superconductivity in diamond *Nature* **428** 542–5
[81] Takano Y, Nagao M, Sakaguchi I, Tachiki M, Hatano T, Kobayashi K, Umezawa H and Kawarada H 2004 Superconductivity in diamond thin films well above liquid helium temperature *Appl. Phys. Lett.* **85** 2851–3
[82] Hebard A F, Rosseinsky M J, Haddon R C, Murphy D W, Glarum S H, Palstra T T M, Ramirez A P and Kortan A R 1991 Superconductivity at 18 K in potassium-doped C60 *Nature* **350** 600
[83] Tanigaki K, Ebbesen T W, Saito S, Mizuki J, Tsai J S, Kubo Y and Kuroshima S 1991 Superconductivity at 33 K in $Cs_xRb_yC_{60}$ *Nature* **352** 222–3
[84] Haddon R C 1992 Electronic structure, conductivity, and superconductivity of alkali metal doped C_{60} *Acc. Chem. Res.* **25** 127–33
[85] Minato J and Miyazawa K 2005 Solvated structure of C_{60} nanowhiskers *Carbon* **43** 2837–41
[86] Cui W *et al* 2011 Synthesis of alkali-metal-doped C_{60} nanotubes *Diam. Relat. Mater.* **20** 93–6

[87] Takeya H, Miyazawa K, Kato R, Wakahara T, Ozaki T, Okazaki H, Yamaguchi T and Takano Y 2012 Superconducting fullerene nanowhiskers *Molecules* **17** 4851–9
[88] Takeya H, Kato R, Wakahara T, Miyazawa K, Yamaguchi T, Ozaki T, Okazaki H and Takano Y 2013 Preparation and superconductivity of potassium-doped fullerene nanowhiskers *Mater. Res. Bull.* **48** 343–5
[89] Murphy D W, Rosseinsky M J, Haddon R C, Ramirez A P, Hebard A F, Tycko R, Fleming R M and Dabbagh G 1991 Superconductivity in alkali metal fullerides *Physica* C **185–9** 403–7
[90] Takeya H, Miyazawa K and Takano Y 2012 Development of alkali-metal doped superconducting fullerene nanowhiskers *Mater. Integr.* **25** 38–44 (in Japanese)
[91] Butterman W C and Reese R G Jr 2003 *Mineral Commodity Profiles—Rubidium* (*US Geological Survey Open-File Report* 03-045)
[92] Wakahara T, Angelo P D', Miyazawa K, Nemoto Y and Ito O 2012 Fullerene/cobalt porphyrin hybrid nanosheets with ambipolar charge transporting characteristics *J. Am. Chem. Soc.* **134** 7204–6
[93] Barzegar H R, Larsen C, Edman L and Wågberg T 2013 Solution-based phototransformation of C_{60} nanorods: towards improved electronic devices *Part. Part. Syst. Charact.* **30** 715–20
[94] Larsen C, Barzegar H R, Nitze F, Wågberg T and Edman L 2012 On the fabrication of crystalline C_{60} nanorod transistors from solution *Nanotechnology* **23** 344015
[95] Doi T, Koyama K, Chiba Y, Tsuji H, Ueno M, Chen S-R, Aoki N, Bird J P and Ochiai Y 2010 Electron transport properties in photo and supersonic wave irradiated C_{60} fullerene nano-whisker field-effect transistors *Japan. J. Appl. Phys.* **49** 04DN12
[96] Cui H *et al* 2014 High-temperature calcined fullerene nanowhiskers as well as long needle-like multi-wall carbon nanotubes have abilities to induce NLRP3-mediated IL-1β secretion *Biochem. Biophys. Res. Commun.* **452** 593–9

Journal of Crystal Growth 416 (2015) 41–46

Contents lists available at ScienceDirect

Journal of Crystal Growth

journal homepage: www.elsevier.com/locate/jcrysgro

Synthesis and structural analysis of C_{60}–C_{70} two-component fullerene nanowhiskers

Toshio Konno, Takatsugu Wakahara, Kun'ichi Miyazawa *

Fullerene Engineering Group, Materials Processing Unit, National Institute for Materials Science (NIMS), 1-1, Namiki, Tsukuba, Ibaraki 305-0044, Japan

ARTICLE INFO

Article history:
Received 17 November 2014
Received in revised form
17 December 2014
Accepted 18 December 2014
Communicated by K. Deppert
Available online 8 January 2015

Keywords:
A1. Spinodal decomposition
B1. Fullerene
C_{60}–C_{70} two-component fullerene nanowhisker
Fullerene nanowhisker
LLIP method

ABSTRACT

C_{60}–C_{70} two-component fullerene nanowhiskers (C_{60}–C_{70}NWs) were synthesized by liquid–liquid interfacial precipitation (LLIP) using various ratios of C_{70} to C_{60} and then analyzed using a focused ion beam processing apparatus (FIB-SEM), scanning electron microscopy (SEM), Raman spectroscopy, ultraviolet-visible (UV-vis) spectroscopy, X-ray diffraction (XRD) and high-performance liquid chromatography (HPLC). Both C_{60} and C_{70} were saturated in the supernatant solutions with fullerene compositions in the mother solutions ranging from 12.4 mass% C_{70} to 73.4 mass% C_{70}. C_{60}–C_{70}NWs contained a small amount of rhombohedral phase, indicating polymerization of C_{60}. The solid solubility limit of C_{70} in the C_{60} matrix was found to be 13.7 mass%. In addition to fine C_{60}–C_{70}NWs, thick C_{60}–C_{70} needle-like crystals were formed. The thick C_{60}–C_{70} needle-like crystals were fractured using a molybdenum probe in the FIB. The fractured surfaces of the C_{60}–C_{70} needle-like crystals showed modulated structures with chemical compositions characteristic of spinodal decomposition. The activation energy of diffusion was determined to be 37.1 kJ/mol.

1. Introduction

Fullerenes were first synthesized by Kroto et al. [1]. Thereafter, efficient methods of fullerene synthesis, such as the arc discharge method [2–4] and the combustion method [5,6], have been developed, and research on fullerenes and fullerene-based materials continue to be conducted throughout the world.

Fullerene molecules bond with each other via van der Waals forces to form molecular crystals. In particular, fullerene needle-like crystals with aspect ratios of 3 or greater and diameters less than 1000 nm are called fullerene nanowhiskers (FNWs) [7,8]. FNWs were first observed in a colloidal solution of PZT containing C_{60} in 2001 [9,10]. In 2002, a liquid–liquid interfacial precipitation method was developed to efficiently synthesize FNWs [11].

FNWs are recyclable, as fullerene molecules can be recovered by redissolving the FNWs into organic solvents such as toluene and benzene. FNWs exhibit semiconductor properties and can potentially be used for field-effect transistors [12], solar cells [13], fuel cells [14,15], catalysts [8,16–20], biosensors [21] and chemical synthesis templates [8].

To date, studies of C_{60} nanowhiskers (C_{60}NWs) have been reported. Because the electrical resistivity of C_{60}NWs is approximately proportional to diameter to the third power [7], the electrical properties of C_{60}NWs vary from insulator to semiconductor depending on diameter. In addition, C_{60}NWs become conductive glass-like carbon nanofibers following high-temperature heat treatment in an inert atmosphere [22]. Additionally, C_{60}NWs can be made into superconductors by doping with alkali metals such as potassium [23,24]. The Young's moduli of C_{60}NWs are 32 to 54 GPa [25], approximately 30 to 60% of the moduli of single-crystal silicon.

Numerous types of FNWs with various new physical properties can be synthesized by combining different fullerene molecules. Synthesis of C_{60}–C_{70} nanowhiskers (C_{60}–C_{70}NWs) was reported in 2004 [26]. The Young moduli of C_{60}–C_{70}NWs were measured by a transmission electron microscope equipped with atomic force microscope functionality and were found to increase with increasing C_{70} content in the mother solutions [27]. This increase in Young's modulus is assumed to be caused by the formation of a C_{60}–C_{70} solid solution that induces hardening, i.e., solid solution hardening. C_{60}–C_{70}NWs have absorption bands of both C_{60} and C_{70}. C_{60}–C_{70}NWs hold potential for semiconductor devices as a new composite material with high Young's moduli and optical properties of both C_{60} and C_{70}.

However, despite the various promising properties of C_{60}–C_{70}NWs, the structural, chemical and optical properties of C_{60}–C_{70}NWs are not well understood. The objective of the present paper is to investigate the structural, chemical and optical properties of these FNWs using a focused ion beam processing apparatus (FIB-SEM), scanning electron microscopy (SEM), X-ray diffraction

* Corresponding author. Tel.: +81298604528; fax: +81298604667.
E-mail address: miyazawa.kunichi@nims.go.jp (K. Miyazawa).

http://dx.doi.org/10.1016/j.jcrysgro.2014.12.016
0022-0248/

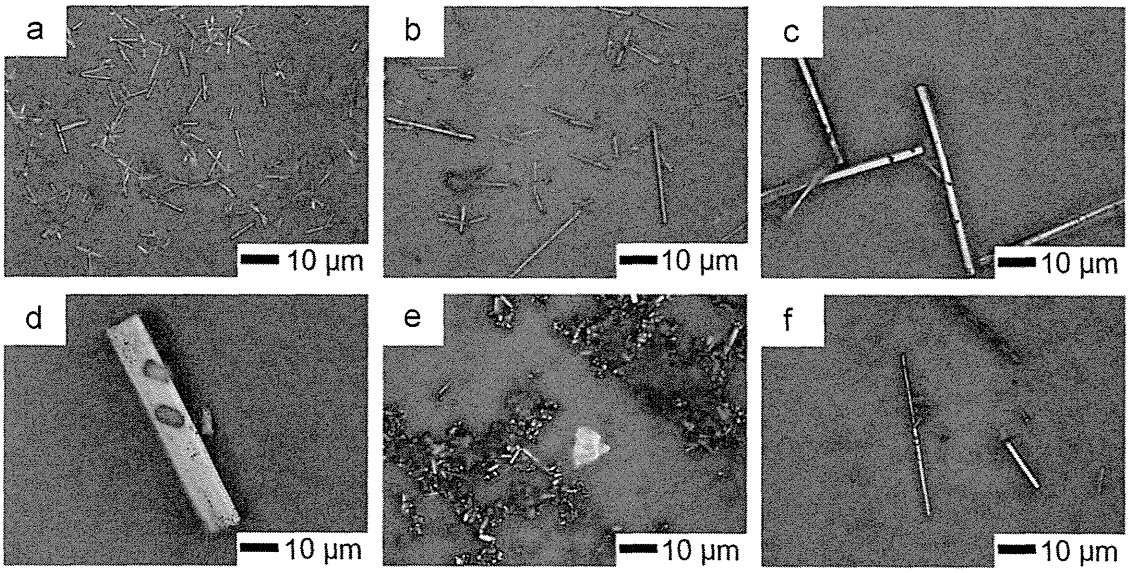

Fig. 1. Optical images of the precipitates. The compositions of mother solutions were (a) C_{60}–9 mass% C_{70}, (b) C_{60}–24 mass% C_{70}, (c) C_{60}–37 mass% C_{70}, (d) C_{60}–45 mass% C_{70}, (e) C_{60}–78 mass% C_{70}, (f) 100 mass% C_{70}.

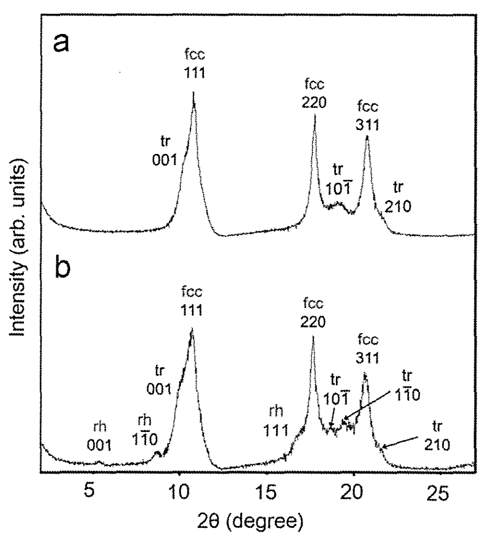

Fig. 2. XRD patterns of (a) the C_{60}NWs and (b) the C_{60}–C_{70}NWs obtained using a mother solution with a composition of C_{60}–24 mass% C_{70}.

(XRD), high-performance liquid chromatography (HPLC), Raman spectroscopy and ultraviolet-visible (UV–vis) spectroscopy.

2. Experimental

Powders of C_{60} (MTR Ltd., 99.5%) and C_{70} (MTR Ltd., 99.0%) were dissolved in toluene (WAKO JIS special grade) by ultrasonic agitation (Iuchi VS-150). The solutions were filtered using syringe filters (MITSUBA HIGH GRADE SYRINGE, Whatman 25 mm GD/X) to generate a C_{60}-saturated toluene solution and a C_{70}-saturated toluene solution.

The C_{60}- and C_{70}-saturated toluene solutions were mixed in various ratios to form C_{60}–C_{70} two-component mother solutions. The mixing ratios were (10.0 mL [C_{60}], 0 mL [C_{70}]), (9.5, 0.5), (9.0, 1.0), (8.5, 1.5), (8.0, 2.0), (7.0, 3.0), (6.0, 4.0), (5.0, 5.0), (4.0, 6.0), (3.0, 7.0), (2.0, 8.0), (1.5, 8.5), (1.0, 9.0), (0.8, 9.2), (0.6, 9.4), (0.5, 9.5), (0.4, 9.6), (0.2, 9.8) and (0, 10.0).

The temperature of each mother solution, stored in glass bottles (volume: 30 mL, inner diameter: 27 mm), was set to 15 °C using a water bath (AS ONE UCT-1000). 10 mL of 2-propanol (WAKO JIS special grade) was slowly layered along the inside wall of the bottle onto an equal volume of fullerene-saturated toluene solution to form a liquid–liquid interface. After forming the interface, the bottle was manually mixed 30 times, then kept still at 15 °C (SANYO MIR-153) for 5 days to complete fullerene precipitation. Then, the supernatant was removed, and 2-propanol was poured into the glass bottle to stabilize the precipitates. After vacuum filtration (KIRIYAMA 5B-21, ULVAC DTC-21), the precipitates were vacuum-dried (AS ONE VO-300) at room temperature.

Structural analysis of specimens was performed by XRD (Rigaku Ultima III) and a FIB-SEM (Hitachi NB5000) equipped with a Ga ion beam source and a field-emission scanning electron microscope (FE-SEM).

Chemical compositions of the specimens was analyzed by HPLC (JASCO UV-2070, PU 2089, CO-2065, LC-Net II/ADC) and Raman spectrometry (JASCO NRS-3000).

The optical properties of the specimens were investigated by ultraviolet–visible spectroscopy (UV–vis, JASCO V-570). The measurement was performed for the vacuum-dried powder of FNWs by the diffuse reflection method using an integrating sphere.

3. Results and discussion

The mother solutions were analyzed by HPLC, the chemical composition of each mother solution was determined.

Fig. 1 shows optical microscope images of the synthesized precipitates with various morphologies and metallic lusters. The images show the formation of fine needle-like crystals (nanowhiskers) in (a), (b) and (f), much bigger needle-like crystals in (c) and (d) and fine granular precipitates in (e).

Fig. 2 shows X-ray diffraction patterns of synthesized C_{60}NWs (a) and of C_{60}–C_{70}NWs synthesized using a mother solution with a composition of C_{60}–24 mass% C_{70} (b). Peaks corresponding to a face-centered cubic (fcc) phase and a triclinic (tr) phase can be assigned in the C_{60}NWs. It is likely that the tr phase was formed by distortion of the fcc phase [28]. The lattice constant of the fcc phase was determined to be $a = 1.422 \pm 0.005$ nm. Peaks corresponding to a rhombohedral phase (rh) in addition to the fcc phase and the tr phase were also observed in the C_{60}–C_{70}NWs. It has been reported that C_{60} can be transformed to a polymer with an rh phase by

Table 1
Lattice constants of C_{60}NWs and C_{60}–C_{70}NWs.

Specimens	Crystal system	Lattice constant (nm)	Primitive unit cell volume (nm^3)
C_{60}NWs	Face-centered cubic (fcc)	$a=1.422\pm0.005$	0.719
	Triclinic (tr)	$a=0.950$, $b=1.000$ $c=1.010$, $\alpha=74.9°$ $\beta=59.4°$, $\gamma=60.0°$	0.715
C_{60}–C_{70}NWs	fcc	$a=1.433\pm0.011$	0.736
	tr	$a=0.951$, $b=0.954$ $c=1.018$, $\alpha=75.4°$ $\beta=60.0°$, $\gamma=60.0°$	0.693
	Rhombohedral (rh)	$a=1.174$, $c=1.652$	0.657

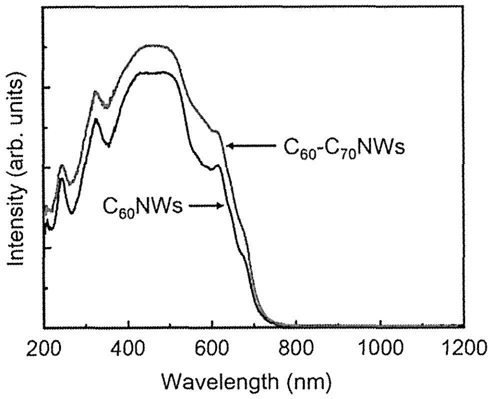

Fig. 3. UV–vis spectra of the C_{60}NWs and the C_{60}–C_{70}NWs obtained using a mother solution with a composition of C_{60}–24 mass% C_{70}.

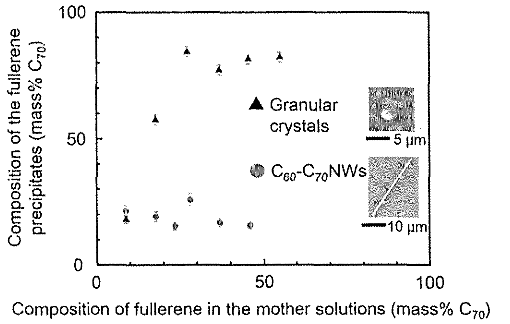

Fig. 4. Chemical composition of the granular crystals and the C_{60}–C_{70}NWs determined by Raman spectroscopy.

high-temperature high-pressure treatment [29]. It is likely that partial polymerization of C_{60} molecules was caused by the addition of C_{70} molecules. The lattice constant of the fcc phase was determined to be $a=1.433\pm0.011$ nm, 0.77% larger than the C_{60}NW lattice constant ($a=1.422\pm0.005$ nm). Table 1 shows the lattice constants and primitive unit cell volumes of C_{60}NWs and C_{60}–C_{70}NWs.

Fig. 3 shows the UV–vis absorption spectra of C_{60}NWs and C_{60}–C_{70}NWs synthesized using a mother solution with a composition of C_{60}–24 mass% C_{70}. The hyperchromic effect and a bathochromic shift were observed for the C_{60}–C_{70}NWs compared to the C_{60}NWs. The C_{60}–C_{70}NWs have a wider light absorption band than the C_{60}NWs, showing stronger absorption especially around 600 nm. This is caused by the wider and stronger absorption range of C_{70} than C_{60} [30].

The composition of C_{60}–C_{70} two-component specimens was measured by Raman spectroscopy and calculated using the peak area ratios, $100\times S_2/(S_1+S_2)$, where S_1 is the peak area of $A_g(2)$ and S_2 is the peak area of $A_1'(6)$ [31]. A linear relationship was assumed to hold between the peak area ratio and the fullerene composition (mass% C_{70}).

Fig. 4 shows the chemical composition of the C_{60}–C_{70}NW surfaces and the granular precipitates as determined by Raman spectroscopy. When the composition of fullerene in the mother solution is 9 mass% C_{70}, the granular precipitates and the C_{60}–C_{70}NWs have similar compositions. However, when the composition of fullerene in the mother solution is at least 18 mass% C_{70}, the composition of fullerene (mass% C_{70}) in the granular crystals is much higher than in the C_{60}–C_{70}NWs. It is likely that the granular precipitates are rich in C_{70} precipitate when the fullerene composition (mass% C_{70}) in the mother solutions exceeds the solid solubility limit of C_{70} in the C_{60} matrix phase.

Chemical composition analysis for the supernatant solutions was performed as shown in Fig. 5. This figure can be divided into three regions (I, II, III). The boundary between I and II is located at 12.4 mass% C_{70}, and the boundary between II and III is located at 73.4 mass% C_{70}. Fig. 5 indicates that the solid solubility of C_{70} in the matrix phase of C_{60} is 12.4 mass% and that the solid solubility of C_{60} in the matrix phase of C_{70} is 26.6 mass%. The chemical compositions of the precipitates determined by HPLC are shown in Fig. 6. Fig. 5 shows that C_{70} is unsaturated in the supernatant solutions for compositions ranging from 0 mass% C_{70} to 12.4 mass% C_{70}, corresponding to region I of Fig. 6. Fig. 5 also shows that C_{60} is unsaturated in the supernatant solutions for compositions ranging from 73.4 mass% C_{70} to 100 mass % C_{70}, corresponding to region III of Fig. 6. Both C_{60} and C_{70} are saturated in the supernatant solutions for compositions ranging from 12.4 mass% C_{70} to 73.4 mass% C_{70}, corresponding to region II of Fig. 6.

Table 2 shows the chemical compositions of the thick C_{60}–C_{70} needle-like crystals determined by HPLC. HPLC analyses of the thick needle-like crystals were performed on individual crystals selected using fine probes. Thick C_{60}–C_{70} needle-like crystals contain 11.1 ± 2.2 mass% C_{70}, up to 13.7 mass% C_{70}. It was found that the solid solubility of C_{70} in the matrix phase of C_{60} is 13.7 mass%. This result corresponds with the result from Fig. 5 (12.4 mass%) as well as previous reports [32,33].

Fig. 7 shows SEM images of a fracture process for a thick C_{60}–C_{70} needle-like crystal synthesized using the mother solution with a composition of C_{60}–45 mass% C_{70}. Image (a) shows a notch formed by sputtering with Ga ion beams and a fixed part by deposition of tungsten (*W*). In images (b), (c) and (d), the C_{60}–C_{70} needle-like crystal was slowly bent by a molybdenum probe and fractured.

Fig. 8 shows SEM images of the fracture surfaces of the C_{60}–C_{70} needle-like crystals. The areas surrounded by the red lines are the areas measured for chemical composition by Raman spectroscopy. Fig. 9 shows the fullerene composition of the fractured surfaces. The fractured surfaces exhibited sinusoidally modulated compositions.

Spinodal decomposition is a phenomenon involving spontaneous biphasic separation, with a sinusoidally modulated structure occurring after a finite time. We believe that these modulated structures result from spinodal decomposition. In Fig. 9, the wavelength of spinodal decomposition is 7.44 ± 2.45 μm. The diffusion length must be comparable to half of the wavelength of spinodal decomposition (3.72 μm). The diffusion length was calculated based on the following equation [34–36]:

$$L=\sqrt{D\times t},\quad D=\frac{1}{6}\times\lambda^2\times\beta\times v_0\times\exp\left(-\frac{Q}{RT}\right),\quad \beta=\exp\left(\frac{S}{k_B}\right)$$

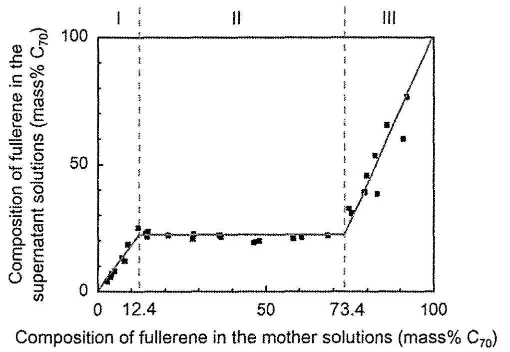

Fig. 5. Chemical composition of the supernatant solutions determined by HPLC.

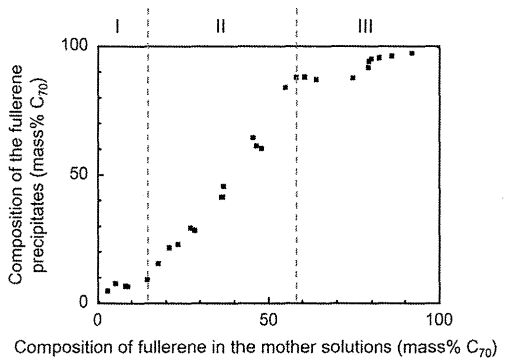

Fig. 6. Chemical composition of the precipitates determined by HPLC.

Table 2
Chemical composition of the thick C_{60}–C_{70} needle-like crystals analyzed by HPLC.

	Mother solution	Thick C_{60}–C_{70} needle-like crystals	
		Average	Maximum
Composition of fullerene (mass% C_{70})	45.4 ± 4.1	11.1 ± 2.2	13.7

where L is the average diffusion length. t is diffusion time, which is 5 days in the present paper. D is the diffusion coefficient. λ is the particle migration length, which is calculated to be $1.433/\sqrt{2}=1.013$ nm using the lattice constant from Table 1. β is the number of microscopic states and ν_0 is the particle vibration frequency. R is the gas constant. S is the entropy and k_B is Boltzmann constant. Q is the activation energy of diffusion, which is equivalent to the binding energy between particles. $L=0.008596 \times \exp(-Q/4789)$ [m], assuming $\beta=1$ and $\nu_0=10^9\,s^{-1}$ for $T=15$ °C. When L equals 3.72 μm, Q is calculated to be 37.1 kJ/mol from Fig. 10.

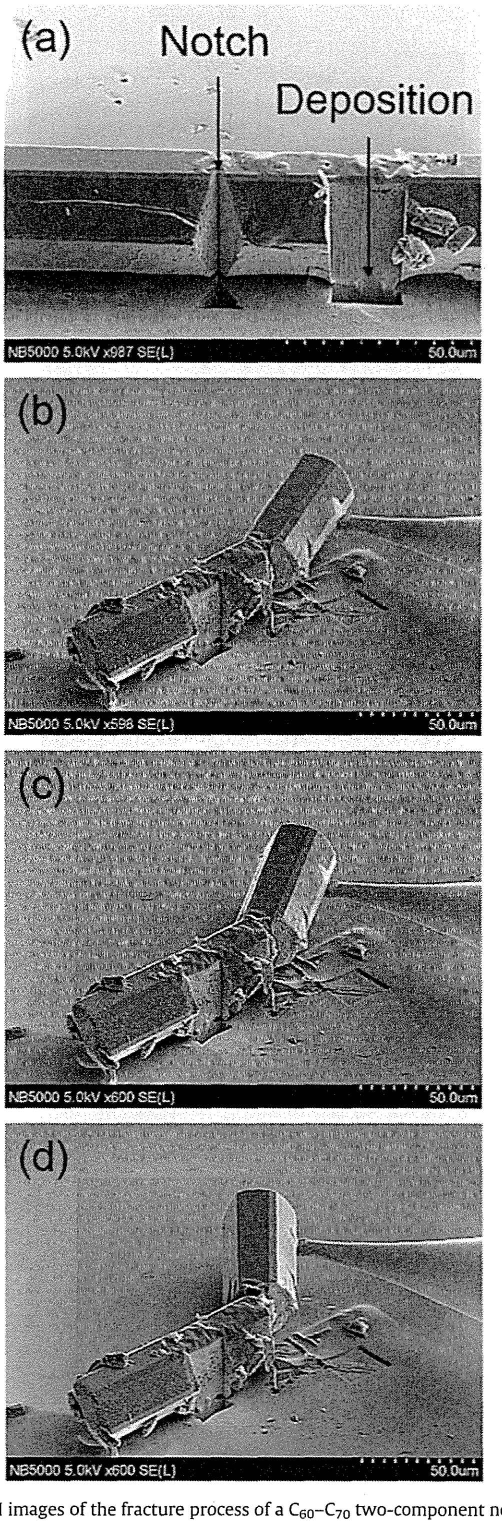

Fig. 7. SEM images of the fracture process of a C_{60}–C_{70} two-component needle-like crystal.

4. Conclusions

(1) The C_{60}–C_{70}NWs contained a small amount of rhombohedral phase and showed an fcc lattice constant that is 0.77% larger than that of C_{60}NWs.
(2) The C_{60}–C_{70}NWs showed a stronger visible light absorption than C_{60}NWs, especially at 600 nm.
(3) Both C_{60} and C_{70} are saturated in the supernatant solutions when the composition of fullerene in the mother solutions ranges from 12.4 mass% C_{70} to 73.4 mass% C_{70}.
(4) The solid solubility limit of C_{70} in the matrix phase of C_{60} is 13.7 mass%.
(5) C_{70} molecules precipitate as granular crystals when the concentration of C_{70} in the mother solutions exceeds the solid solubility limit of C_{70} in C_{60}.
(6) The fractured surfaces of C_{60}–C_{70} needle-like crystals showed modulated structures and chemical compositions, indicating spinodal decomposition. The activation energy of diffusion was calculated to be 37.1 kJ/mol.

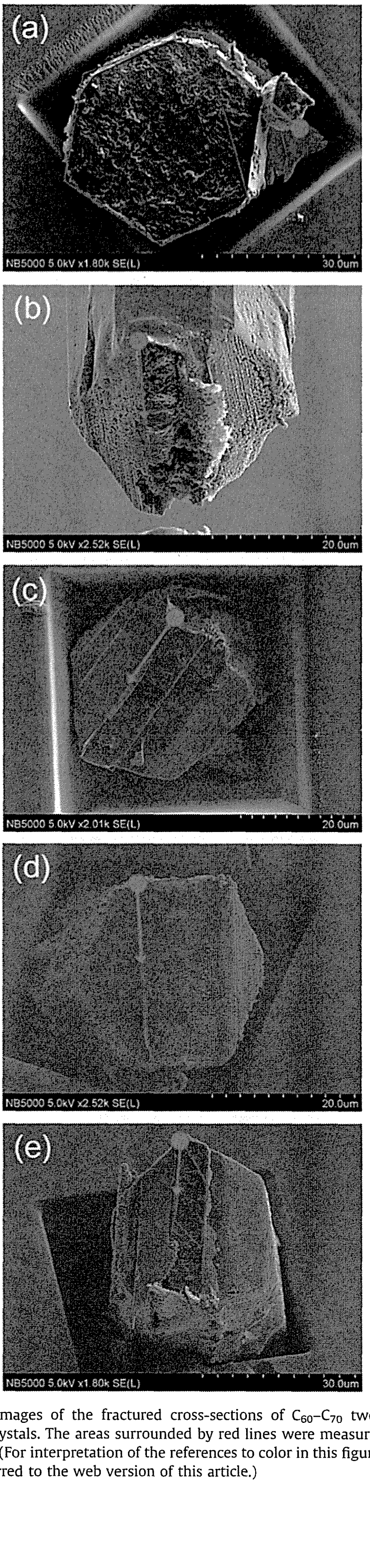

Fig. 8. SEM images of the fractured cross-sections of C_{60}–C_{70} two-component needle-like crystals. The areas surrounded by red lines were measured by Raman spectroscopy. (For interpretation of the references to color in this figure legend, the reader is referred to the web version of this article.)

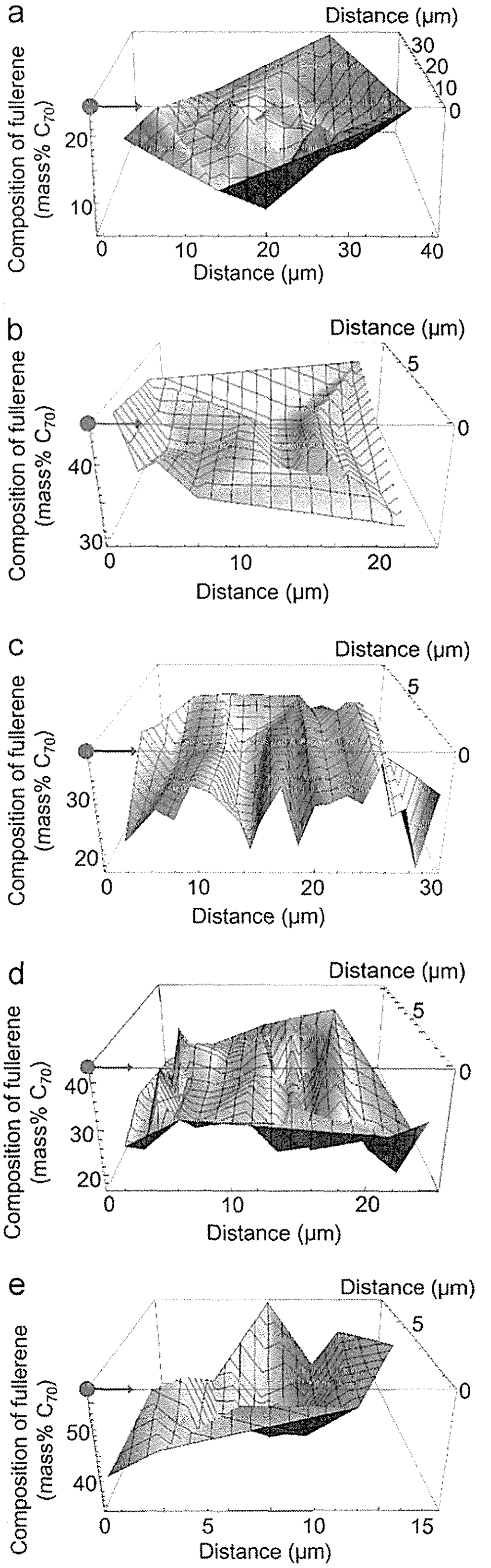

Fig. 9. Chemical composition of the fractured cross-sections of C_{60}–C_{70} needle-like crystals. (a)–(e) in the figure correspond to (a)–(e) in Fig. 8, respectively. The red arrows and circles in the figure correspond to those in Fig. 8. (For interpretation of the references to color in this figure legend, the reader is referred to the web version of this article.)

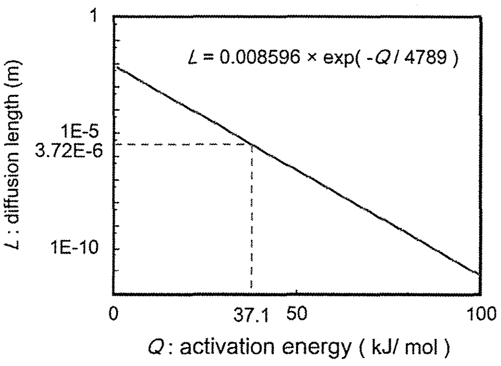

Fig. 10. Relationship between the diffusion length and the activation energy of C_{60} molecules calculated using $t=5$ days, $\lambda=1.013$ nm, $\beta=1$, $\nu_0=10^9\ s^{-1}$ and $T=15$ °C.

Acknowledgments

Portions of this research were supported by the Health and Labor Sciences Research Grants (H24-Chemistry-Shitei-009) from the Ministry of Health, Labor and Welfare of Japan, the JST Strategic Japanese-EU Cooperative Program "Study on managing the potential health and environmental risks of engineered nanomaterials", the Center of Materials Research for Low Carbon Emission of NIMS, and JSPS KAKENHI Grant number 26600007.

References

[1] H.W. Kroto, J.R. Heath, S.C. O'Brien, R.F. Curl, R.E. Smalley, Nature 318 (1985) 162–163.
[2] R.E. Haufler, J. Conceicao, L.P.F. Chibante, Y. Chai, N.E. Byrne, S. Flanagan, M.M. Haley, S.C. O'Brien, C. Pan, Z. Xiao, W.E. Billups, M.A. Ciufolini, R. H. Hauge, J.L. Margrave, L.J. Wilson, R.F. Curl, R.E. Smalley, J. Phys. Chem. 94 (1990) 8634.
[3] W. Krätschmer, L.D. Lambt, K. Fostiropoulos, D.R. Huffmant, Nature 347 (1990) 354.
[4] H. Ajie, M.M. Alvarez, S.J. Anz, R.D. Beck, F. Diedrich, K. Fostiropoulos, D.R. Huffman, W. Krätschmer, Y. Rubin, K.E. Shriver, D. Sensharma, R. L. Whetten, J. Phys. Chem. 94 (1990) 8630.
[5] J.B. Howard, J.T. McKinnon, M.E. Johnson, Y. Makarovsky, A.L. Lafleur, J. Phys. Chem. 96 (1992) 6657.
[6] J.B. Howard, J.T. McKinnon, Y. Makarovsky, A.L. Lafleur, M.E. Johnson, Nature 352 (1991) 139.
[7] Fullerene Nanowhiskers, in: K. Miyazawa (Ed.), Pan Stanford Publishing Pte. Ltd, Singapore, 2011.
[8] K. Miyazawa, J. Nanosci. Nanotechnol. 9 (2009) 41–50.
[9] K. Miyazawa, A. Obayashi, M. Kuwabara, J. Am. Ceram. Soc. 84 (2001) 3037–3039.
[10] K. Rauwerdink, J. Liu, J. Kintigh, G.P. Miller, Microsc. Res. Tech. 70 (2007) 513.
[11] K. Miyazawa, Y. Kuwasaki, A. Obayashi, M. Kuwabara, J. Mater. Res. 17 (2002) 83–88.
[12] K. Ogawa, T. Kato, A. Ikegami, H. Tsuji, N. Aoki, Y. Ochiai, J.P. Bird, Appl. Phys. Lett. 88 (2006) 112109.
[13] P.R. Somani, S.P. Somani, M. Umeno, Appl. Phys. Lett. 91 (2007) 173503.
[14] K. Miyazawa, J. Minato, H. Zhou, T. Taguchi, I. Honma, T. Suga, J. Eur. Ceram. Soc. 26 (2006) 429.
[15] Q. Wang, Y. Zhang, K. Miyazawa, R. Kato, K. Hotta, T. Wakahara, J. Phys. Conf. Ser. 159 (2009) 012023.
[16] M. Sathish, K. Miyazawa, T. Sasaki, Chem. Mater. 19 (2007) 2398.
[17] M. Sathish, K. Miyazawa, T. Sasaki, J. Solid State Electrochem. 12 (2008) 835.
[18] M. Sathish, K. Miyazawa, T. Sasaki, Diamond Relat. Mater. 17 (2007) 571.
[19] M. Sathish, K. Miyazawa, Nano 3 (19) (2008) 409.
[20] B.H. Cho, K.B. Lee, K. Miyazawa, W.B. Ko, Asian J. Chem. 25 (2013) 8027.
[21] X. Zhang, Y. Qu, G. Piao, J. Zhao, K. Jiao, Mater. Sci. Eng., B 175 (2010) 159.
[22] K. Asaka, T. Nakamura, K. Miyazawa, Y. Saito, Surf. Interface Anal. 44 (2012) 780.
[23] H. Takeya, K. Miyazawa, R. Kato, T. Wakahara, T. Ozaki, H. Okazaki, T. Yamaguchi, Y. Takano, Molecules 17 (2012) 4851.
[24] H. Takeya, R. Kato, T. Wakahara, K. Miyazawa, T. Yamaguchi, T. Ozaki, H. Okazaki, Y. Takano, Mater. Res. Bull. 48 (2013) 343.
[25] K. Asaka, R. Kato, K. Miyazawa, T. Kizuka, Appl. Phys. Lett. 89 (2006) 071912.
[26] K. Miyazawa, M. Fujino, J. Minato, T. Yoshii, T. Kizuka, T. Suga, Structure and properties of fullerene nanowhiskers prepared by the liquid–liquid interfacial precipitation method, in: Proc. SPIE 5648, Smart Materials III, P. 224, Smart Materials, Nano-, and Micro- Smart Systems 2004, 12–15 December 2004, Sydney, Australia.
[27] D. Matsuura, T. Konno, T. Wakahara, K. Miyazawa, T. Kizuka, Young's modulus of C_{60}/C_{70} alloy nanowhiskers, in: Abstracts of 2014 Tsukuba Nanotechnology Symposium (TNS'14), July 25–26, 2014, University of Tsukuba, Tsukuba, Japan.
[28] K. Miyazawa, H. Satsuki, M. Kuwabara, M. Akaishi, J. Mater. Res., 16 (2001) 1960.
[29] Y. Iwasa, T. Arima, R.M. Fleming, T. Siegrist, O. Zhou, R.C. Haddon, L.J. Rothberg, K.B. Lyons, H.L. Carter Jr., A.F. Hebard, R. Tycko, G. Dabbagh, J.J. Krajewski, G.A. Thomas, T. Yagi, Science 264 (1994) 1570.
[30] S. Pfuetzner, J. Meiss, A. Petrich, M. Riede, K. Leo, Appl. Phys. Lett. 94 (2009) 223307.
[31] R. Meilunas, R.P.H. Chang, S. Liu, M. Jensen, M.M. Kappes, J. Appl. Phys. 70 (1991) 5128.
[32] D. Havlik, W. Schranz, M. Haluška, H. Kuzmany, P. Rogl, Solid State Commun. 104 (1997) 775.
[33] K. Miyazawa, J. Minato, J. Mater. Res. 20 (2005) 688.
[34] M. Vos, P.L. Grande, D.K. Venkatachalam, S.K. Nandi, R.G. Elliman, Phys. Rev. Lett. 112 (2014) 175901.
[35] S. Kawasaki, E. Sakai, J. Nucl. Sci. Technol. 4 (1967) 273.
[36] E. Fujita, Kinzoku Butsuri -Zairyou Kagaku no Kiso-, Agne 661 (1996) (in Japanese).

液-液界面析出法(LLIP 法)によるフラーレンのナノウィスカー・ナノチューブ・ナノシートの合成*

宮 澤 薫 一**

1 はじめに

C_{60} が 1985 年に発見されてより[1]，C_{60} のみならず C_{70} や内包フラーレンを用いた様々な形状の分子結晶が合成されている．筆者らは 2001 年にチタン酸ジルコン酸鉛のコロイド溶液中に C_{60} を添加する研究において C_{60} フラーレンナノウィスカーを見出して以来[2]，液-液界面析出法(liquid-liquid interfacial precipitation method, LLIP 法)によって[3]，様々な形状のフラーレン結晶の合成を行っている．本稿では，筆者らが開発した LLIP 法の原理と LLIP 法によるファイバーおよびシート状のフラーレン結晶の合成例について述べる．

2 液-液界面析出法(LLIP 法)

液-液界面析出法とは，フラーレンの良溶媒(A)の飽和溶液①にフラーレンの貧溶媒(B)を重層し，この過飽和となった液-液界面において生じるフラーレン結晶核の析出と，さらなる良溶媒-貧溶媒の相互拡散によるフラーレンの過飽和状態の維持によって，フラーレン結晶核の成長を行わせる方法である[3],[4]．良溶媒 A と貧溶媒 B は互いに混和するものを用いるが，図 1 に示す LLIP 法においては，①に B を，B を①に重層しても良い．あるいは，B の内部に①を注入しても，逆に，①の内部に B を注入しても良く，さらにまた，B に①を，①を B に滴下する形で添加しても良い．重要なことは，①と B の 2 液を合わせる過程においては，必ず液-液界面が形成され(図 1(a))，その界面における相互拡散によってフラーレンの過飽和状態が生じ(図 1(b))，フラーレン結晶核が発生する現象を用いることが，LLIP 法の意図するところである．LLIP 法は，実質的には 2 液を混合する方法であるが，図 1(a)のように，液-液界面をひとつだけ形成するときのみならず，図 1(c)のように，注入などの方法によって導入された小さな貧溶媒体積 B の周りに，溶液①と貧溶媒 B の液-液界面が必然的に

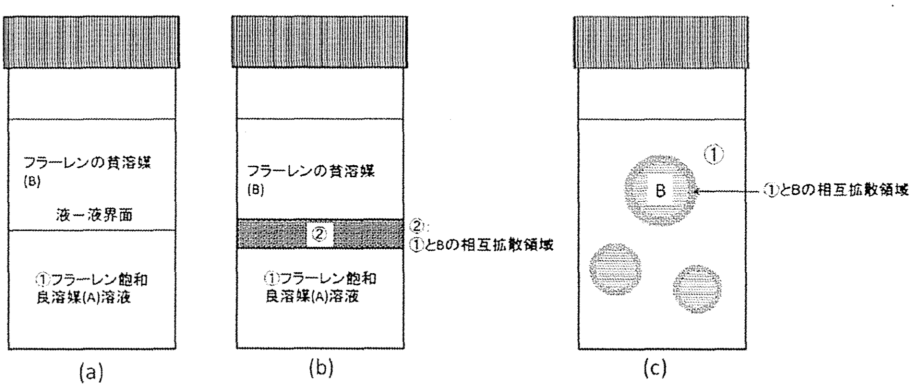

図 1　(a)フラーレンを飽和させた良溶媒(A)溶液①に，フラーレンの貧溶媒(B)を重層した模式図，(b)溶液①と貧溶媒 B との相互拡散領域②，(c)溶液①の中に溶媒 B を注入して生じる球状の領域と溶液①との液-液界面において，過飽和領域が生じることを示す模式図

* Synthesis of Fullerene Nanowhiskers, Fullerene Nanotubes and Fullerene Nanosheets by Liquid-Liquid Interfacial Precipitation (LLIP) Method

** Kun'ichi MIYAZAWA

生じ，引き続き起こる相互拡散によって過飽和領域が形成されるため，このような場合をも含めてLLIP法と呼んでいる．図1のように液-液界面を形成しそのまま拡散と結晶成長を行わせる方法を静置液-液界面析出法(static liquid-liquid interfacial precipitation method，静置LLIP法)とも呼ぶ[4]．

3 フラーレンナノウィスカーの合成

フラーレンナノウィスカー(fullerene nanowhisker, FNW)とは，フラーレン分子から成る細いファイバー状結晶(ウィスカー)であって，直径が1000 nm未満のものである[5]．LLIP法を用いて，C_{60}(フラーレン)ナノウィスカー，C_{70}(フラーレン)ナノウィスカー[2)-6),8)]のようなFNWの他に，C_{60} [$C(COOC_2H_5)_2$] のようなフラーレンの誘導体を用いたFNWの合成も可能である[7),9),10)]．また，LLIP法を用いて，C_{60}母相中にC_{70}を固溶させたFNWや，C_{60}母相中にC_{60} [$C(COOC_2H_5)_2$] や$C_{60}C_3H_7N$を固溶させた複数種類のフラーレン分子から成るFNWを合成することも可能である[9),10)]．

図2にC_{60}母相中にC_{60} [$C(COOC_2H_5)_2$] を固溶させたC_{60}–C_{60} [$C(COOC_2H_5)_2$] 2成分ナノウィスカーの透過電子顕微鏡(TEM)像を示す[10)]．

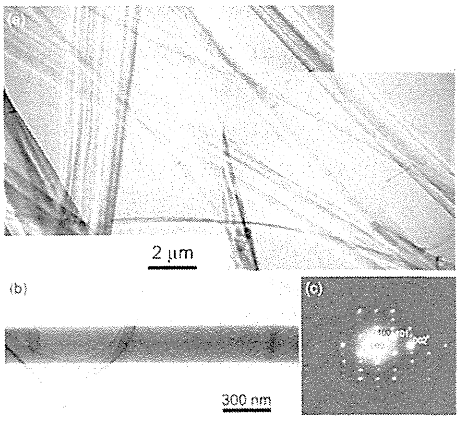

図2 (a)C_{60}–4.1 mol% C_{60} [$C(COOC_2H_5)_2$] 粉末を用いて合成された2成分FNWのTEM像，(b)同FNW一部のTEM像とその電子線回折図形(c)[10)]

4 フラーレンナノチューブの合成

フラーレンナノウィスカーは，中空でないフラーレンの細い針状結晶であるのに対して，フラーレンナノチューブ(FNT)とは，フラーレン分子から構成される中空の針状物質である．FNTは，陽極酸化アルミナ膜(AAO膜)の膜孔中にC_{60}のトルエン溶液を侵入させ，それを乾燥，焼成するというプロセスを経て，膜孔の内壁をC_{60}でコーティングし，最後に化学的処理によってアルミナ膜を溶解除去することによって中空の構造をもつ針状物質が合成された[11)]．このようにして合成されるC_{60}ナノチューブ(C_{60}NT)の直径はAAO膜孔の大きさによって規定された揃った直径をもつという利点があるが，多結晶や非晶質構造のものであった．一方，筆者らはC_{70}のピリジン飽和溶液とイソプロピルアルコール(IPA)の静置LLIP法によって，単結晶の壁構造をもつファイバー状のC_{70}ナノチューブ(C_{70}NT)の合成に成功した[12),17)]．同時に，C_{70}を約15 mol%固溶させた単結晶の壁構造をもつC_{60}–C_{70} 2成分ナノチューブの合成にも成功した[12)]．C_{60}NTは，C_{60}のピリジン飽和溶液とIPAの静的LLIP法により合成することができるが[13)]，収率を向上させるため，紫外線や青色光で照射したC_{60}飽和ピリジン溶液を用いて，液-液界面を形成後，超音波照射を施すことによってC_{60}NTを合成する方法を開発した[14)]．この方法は，静置LLIP法に超音波による強制混合プロセスを付加した方法であるので，強制混合液-液界面析出法(forced mixing liquid-liquid interfacial precipitation method，強制混合LLIP法)と呼んでいる．

今日まで様々なFNWやFNTがLLIP法によって合成されており，FNWとFNTをひとまとめにしてフラーレンナノファイバーとも呼んでいる[15),16)]．

図3にC_{60}NTの光学顕微鏡像とTEM像[14)]を，**図4**にC_{70}NTのTEM像を示す[12)]．

5 フラーレンナノシートの合成

Sathishらはフラーレンの良溶媒と貧溶媒の組合せを適当に選択することにより，ファイバー状のみならず薄いシート状の物質を合成した[18)]．これをフラー

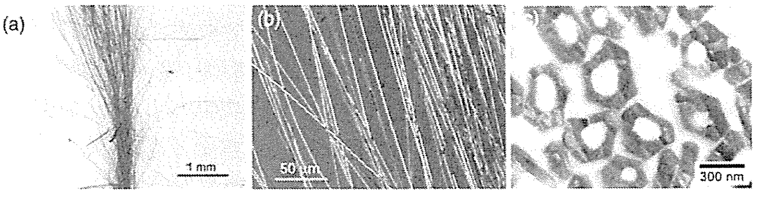

図3 C_{60}NTの光学顕微鏡像(a)，(b)と，C_{60}NTの断面TEM像(c)[14)]

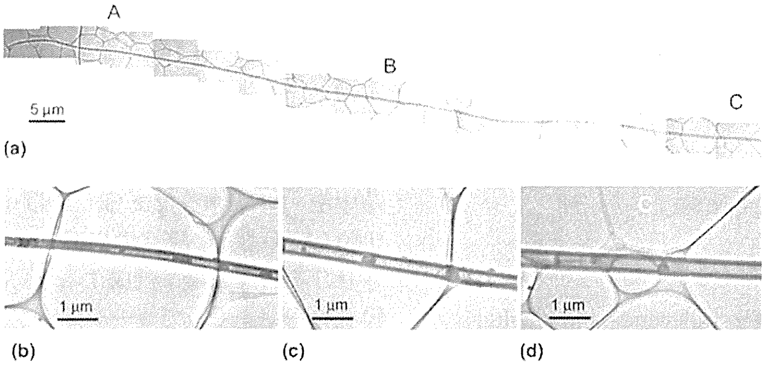

図4　C_{70}NT の TEM 像(a)と，A, B, C 部分の拡大像(b), (c), (d)[12]

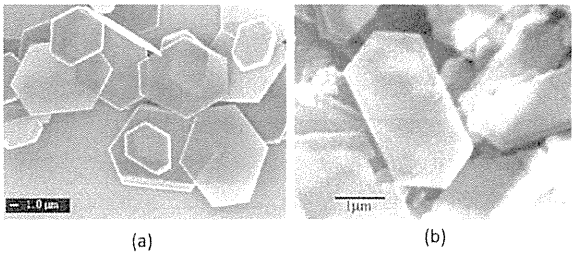

図5　(a)C_{60} ナノシート[19]と(b)C_{70} ナノシート[20]の SEM 像

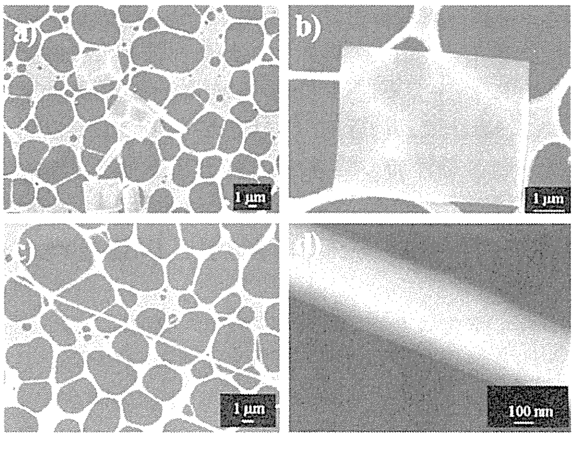

図6　$Sc_3N@C_{80}$ ナノシートの SEM 像 a), b). $Sc_3N@C_{80}$ ナノウィスカーの SEM 像 c)と拡大像 d)[21]

レンナノシートと呼んでいる．次いで若原らによって，LLIP 法においてフェロセンを添加することによりフラーレンナノシートの合成が容易にできることが発見された[19]．図5(a)に C_{60} ナノシートの[19]，図5(b)に C_{70} ナノシート[20]の走査電子顕微鏡(SEM)像を示す．このC$_{60}$ ナノシートは，C_{60} とフェロセンのトルエン溶液と IPA の LLIP 法により合成されたもの[19]，また，C_{70} ナノシートは，C_{70} とフェロセンのトルエン溶液と IPA の LLIP 法によって合成されたものである[20]．

図6に，内包フラーレン $Sc_3N@C_{80}$ と CS_2 および IPA を用いて，LLIP 法により合成された $Sc_3N@C_{80}$ ナノシートと $Sc_3N@C_{80}$ ナノウィスカーの走査電子顕微鏡(SEM)像を示す[21]．

Co ポルフィリン(5,10,15,20-tetrakis(4-methoxyphenyl) porphyrinato cobalt(II), CoTMPP))を添加した C_{60} ナノシートも合成された[22]．この合成は，C_{60} と CoTMPP のトルエン溶液と IPA の LLIP 法による．CoTMPP 添加 C_{60} ナノシートを用いてアンバイポーラ特性を示す電界効果トランジスター(FET)が作製された．CoTMPP 添加 C_{60} ナノシートの厚さは，原子間力顕微鏡(AFM)の測定により約 50～200 nm であった[22]．

6　垂直配向フラーレンマイクロチューブの合成

陽極酸化アルミナ膜(AAO)の膜孔を通じて，C_{60} 飽和トルエン溶液に IPA をゆっくりと注入することにより，アルミナ膜上に，直径がマイクロメートルサイズの C_{60}(フラーレン)マイクロチューブ(C_{60}MT)を合成することができる[23,24]．図7にその合成方法(diaphragm liquid-liquid interfacial precipitation (DLLIP) method，隔膜液-液界面析出法[24])と C_{60}MT の SEM 像を，図8に集束イオンビーム加工観察装置(FIB-SEM, Hitachi NB5000)による観察例と，図9に C_{60}MT の縦断面 SEM 像を示す．C_{60}MT は AAO 膜上に約 400～500 μm の長さにまで成長している．成長軸方向に沿っての観察像からわかるように(図7(c))，C_{60}MT は六角柱の断面形状をもつ柱状晶である．図9は，C_{60}MT と AAO 膜の接合部近傍では中空でないが，成長するにつれて中空部が形成されることを示している．これは C_{60}MT の外表面の成長速度が大きいために内部への C_{60} の供給が十分でなく中空構造が形成されたと考察することができる．成長に伴って溶液中の C_{60} は消費されて C_{60} 濃度が減少することを考慮すると，C_{60} 濃度の減少によって内部への C_{60} の供給が十分に行われないために中空構造が形成されたと推察している．また，C_{60} の過飽和状態を

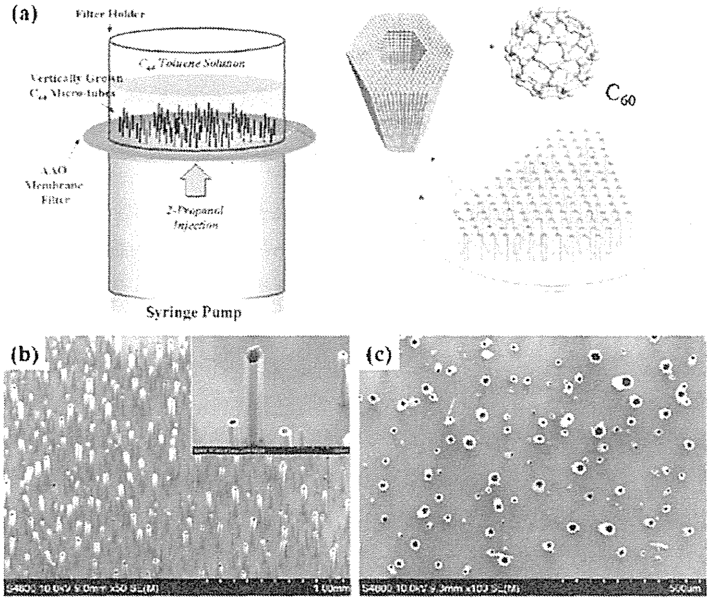

図7　AAO 膜の膜孔を通して C_{60} 飽和トルエン溶液中に IPA を注入する DLLIP 法による C_{60}MT の合成方法の模式図(a)と，垂直配向 C_{60}MT の SEM 像(b)，(c)[23]

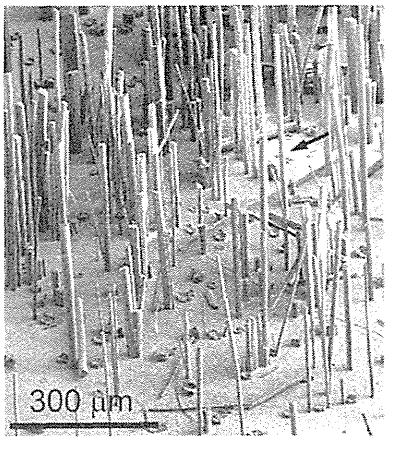

図8　DLLIP 法により AAO 膜上に合成された垂直配向 C_{60}MT の SEM 像[24]

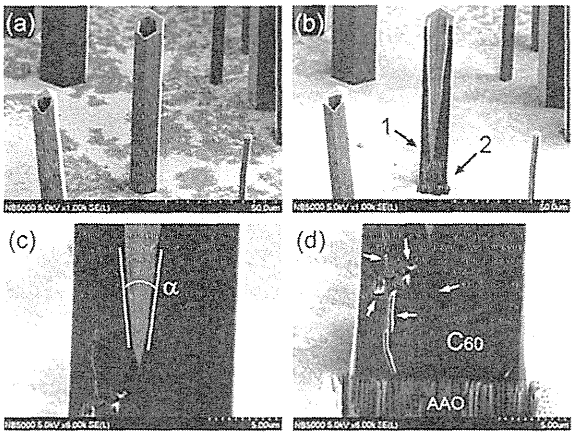

図9　C_{60}MT の SEM 像(a)，(a)の中央の C_{60}MT を Ga イオンビームで加工して縦断面を形成した C_{60}MT の SEM 像(b)，(b)の矢印1で示した近傍の拡大像(c)，AAO 膜と C_{60}MT 接合界面近傍の SEM 像(d)[24]
角度 $\alpha = 14°$．図(d)の矢印は空隙を示す．

もたらす IPA は C_{60} 結晶核の外側から供給されるので，結晶表面に比べて針状結晶内部の成長が遅れることが考えられる．さらに，C_{60}MT の成長に伴って溶液中における C_{60} は消費されるため，この結果生じる C_{60} 濃度の減少は C_{60} 針状結晶コア部分の再溶解を引き起して中空構造を形成することも考えられる[30]．C_{60}MT の成長には，上記のプロセスが複雑に寄与していると考察される．

C_{60}NT や C_{70}NT などの FNT の形成においても，外表面先端部における成長速度に対して，溶液中におけるフラーレン濃度の減少によって，内部へのフラーレンの供給と結晶化が十分な速さで行われないために中空構造が形成されると考えられる[25]．図4の C_{70}NT の TEM 像で示すように[12]，C_{70}NT の端部は閉じた構造をもっており，図4(b)の矢印で示された場所から中空構造が形成されている．これは上記の考察を裏付けている．また，C_{70}NT の内部から溶出したような例も観察されているため[12]，C_{70}NW の中央部分の溶解による中空構造の形成(コア溶解モデル)も考えられる．従って，FNT の形成は，フラーレン分子の結晶表面への供給とその結晶化過程，および，内部コア溶解過程の因子が複雑に関係して生じていると推察される．

7　フラーレンナノウィスカーの成長に及ぼす溶液体積の影響

C_{60}NW の成長には，温度，水，フラーレンの良溶媒と貧溶媒の組合せと組成[4]，および光[26]が影響することがわかっている．最近，竹屋らによりカリウム(K)を添加した数マイクロメートル長の短い C_{60}NW が，超伝導体積分率 80％程度となる良好な超伝導体となることが発見された[27),28]．K 添加 C_{60}NW 超伝導体は，その超伝導転移温度(T_c)は約 17 K であって液体窒素温度レベルではないが，高磁場まで 30 万 A・cm^{-2} 以上の高い超伝導臨界電流密度(J_c)を維持し，かつ，密度が約 2 g・cm^{-3} 程度であってたいへん軽いという特徴を有している．この短い C_{60}NW は C_{60} 飽和トルエン溶液と IPA の組合せによる強制混合 LLIP 法によって作製したものである．強制混合 LLIP 法による C_{60}NW の成長機構を探るために，溶液体積と C_{60}NW のサイズがどのような関係になるのかを研究した[29]．

異なった内径のガラスびんを 5 種類用意し，それぞれについて，C_{60} 飽和トルエン溶液に等体積の IPA を重層して液-液界面を形成後，30 回手振り混合して核生成させたのち，15℃ で 8 日間低温恒温器に保管した．図10に示すように直線性の良い C_{60}NW が合成された．図11(a)，(b)，(c)に，各ガラスびんにおける C_{60}NW の平均長さ，平均直径，平均アスペクト比(長さ/直径)と溶液体積との関係を示す．溶液体積をゼロに外挿して得られる各切片の値は，C_{60}NW 結晶

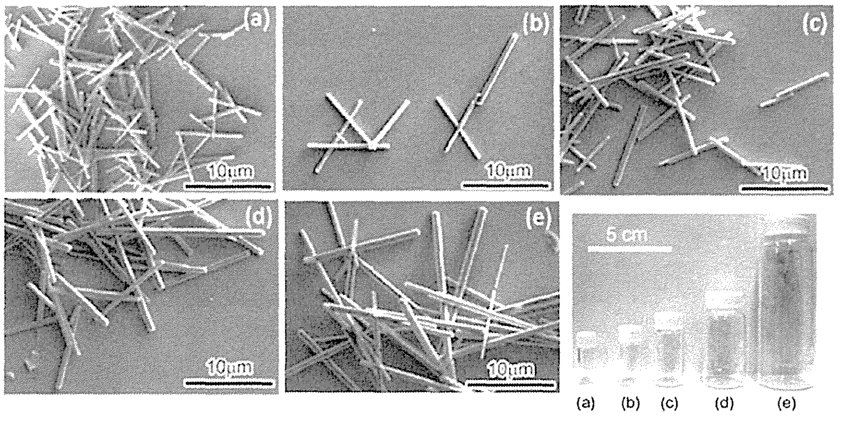

図10　異なった内径のガラスびんで合成された C_{60}NW の SEM 像[29]
びん内径：(a)10.0 mm，(b)12.5 mm，(c)18.0 mm，(d)27.0 mm，(e)36.5 mm.
各びんの溶液体積は，(a)1.5 cm^3，(b)3.0 cm^3，(c)8.0 cm^3，(d)20.0 cm^3，(e)80.0 cm

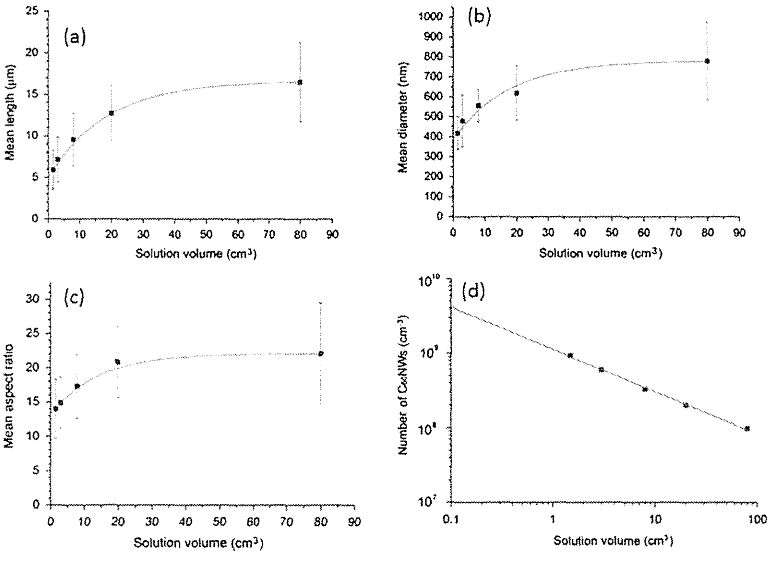

図11　異なったサイズのびんで合成した C_{60}NW の平均長さ(a)，平均直径(b)，アスペクト比(c)，溶液中の数密度(d)と溶液体積との関係[29]

核の平均の大きさとアスペクト比を表していると考えられる．平均長さの切片は 5.02 μm，平均直径の切片は 387 nm であり，アスペクト比＝5.02 μm/387 nm＝13.0 となる．一方，図 11(c)の切片から求められるアスペクト比は 13.1 であり，これは長さと直径の切片から求められたアスペクト比 13.0 と良く一致している．このことは溶液体積をパラメータ(x)とした C_{60}NW サイズの解析が正しいことを裏付けている．また，各ガラスびんにおける C_{60}NW の平均長さと平均直径を用いて C_{60}NW の平均質量(乾燥時)を計算し，C_{60} の仕込み量から本数を算出して，溶液の単位体積当たりの C_{60}NW の本数(数密度)を計算したものを図 11(d)に示す．C_{60}NW の数密度(y)の当てはめ曲線は，$y=1.12496\times10^{9}/x^{0.5674}$，となった．これは，$C_{60}$NW の溶液中における数密度が，ほぼ溶液体積の平方根に反比例して変化することを示している．

8 まとめ

液-液界面析出法(LLIP 法)によって，ナノウィスカー，ナノチューブ，ナノシート，マイクロチューブなどのフラーレンナノマテリアルを作りわけることができる．これらは半導体であってトランジスタ，光センサーなどの多数種類の電子デバイスの作製に利用することができる．中でも，C_{60}NW にアルカリ金属を添加して超伝導体とすることに成功した．これはリニア形状の炭素が初めて超伝導体となった例である．フラーレンナノマテリアルの応用にはサイズ制御技術を確立することが必要であり，成長メカニズムの研究を進めている．最近，良好な超伝導特性を示した短い C_{60}NW の大きさが，溶液体積の関数として整理できることが見出された．C_{60}NW の成長は溶媒の種類にも影響されるので，成長機構の解明には一層の研究が必要であるが，上記の方法は C_{60}NW の生成核のサイズと数を制御するために有用であろう．本稿以外においても，LLIP 法で合成されたフラーレン結晶は多数あり，それらの構造や物性は文献 31 に詳述されている．

謝　辞

本研究の一部は，厚生労働科学研究費補助金(化学物質リスク研究事業)「ナノマテリアル曝露による生体毒性の慢性移行および遅発性に関わる評価手法の開発研究(H24-化学-指定-009)」，JSPS 科研費 26600007，低炭素研究ネットワーク，及び，NIMS 内プロジェクト「新材料創出を可能にする粒子プロセスの開発と応用(代表：目　義雄)」の支援を受けて行われた．

文　献

1) H. W. Kroto, J. R. Heath, S. C. O'Brien, R. F. Curl, R. E. Smalley, *Nature*, **318**, 162–163 (1985).
2) K. Miyazawa, A. Obayashi, M. Kuwabara, *J. Am. Ceram. Soc.*, **84**, 3037–3039 (2001).
3) K. Miyazawa, Y. Kuwasaki, A. Obayashi, M. Kuwabara, *J. Mater. Res.*, **17**, 83–88 (2002).
4) K. Miyazawa, K. Hotta, *J. Cryst. Growth*, **312**, 2764–2770 (2010).
5) K. Miyazawa, *J. Nanosci. Nanotechnol.*, **9**, 41–50 (2009).
6) K. Miyazawa, *J. Am. Ceram. Soc.*, **85**, 1297–1299 (2002).
7) K. Miyazawa, T. Mashino, T. Suga, *J. Mater. Res.*, **18**, 2730–2735 (2003).
8) K. Miyazawa, C. Nishimura, M. Fujino, T. Suga, T. Yoshii, *Trans. Mater. Res. Soc. Jpn.*, **29**, 1965–1968 (2004).
9) K. Miyazawa, T. Mashino, T. Suga, *Trans. Mater. Res. Soc. Jpn.*, **29**, 537–540 (2004).
10) K. Miyazawa, J. Minato, T. Mashino, S. Nakamura, M. Fujino, T. Suga, *NUKLEONIKA*, **51** Supplement 1, S41–S48 (2006).
11) H. Liu, Y. Li, L. Jiang, H. Luo, S. Xiao, H. Fang, H. Li, D. Zhu, D. Yu, J. Xu, B. Xiang, *J. Am. Chem. Soc.*, **124**, 13370–13371 (2002).
12) K. Miyazawa, J. Minato, T. Yoshii, M. Fujino, T. Suga, *J. Mater. Res.*, **20**, 688–695 (2005).
13) J. Minato, K. Miyazawa, T. Suga, *Sci. Technol. Adv. Mater.*, **6**, 272–277 (2005).
14) K. Miyazawa, C. Ringor, *Mater. Lett.*, **62**, 410–413 (2008).
15) K. Miyazawa, T. Mashino, T. Suga, *J. Mater. Res.*, **18**, 2730–2735 (2003).
16) K. Miyazawa, J. Nanosci. *Nanotechnol.*, **9**, 41–50 (2009).
17) K. Miyazawa, J. Minato, T. Yoshii, T. Suga, *Sci. Technol. Adv. Mater.*, 6, 388–393 (2005).
18) M. Sathish, K. Miyazawa, *J. Am. Chem. Soc.*, **129**, 13816–13817 (2007).
19) T. Wakahara, M. Sathish, K. Miyazawa, C. Hu, Y. Tateyama, Y. Nemoto, T. Sasaki, O. Ito, *J. Am. Chem. Soc.*, **131**, 9940–9944 (2009).

20) K. Osonoe, R. Kano, K. Miyazawa, M. Tachibana, *J. Cryst. Growth*, **401**, 458–461 (2014).
21) T. Wakahara, Y. Nemoto, M. Xu, K. Miyazawa, D. Fujita, *Carbon*, **48**, 3359–3363 (2010).
22) T. Wakahara, P. D'Angelo, K. Miyazawa, Y. Nemoto, O. Ito, *J. Am. Chem. Soc.*, **134**, 7204–7206 (2012).
23) S. I. Cha, K. Miyazawa, J.-D. Kim, *Chem. Mater.*, **20**, 1667–1669 (2008).
24) K. Miyazawa, R. Kuriyama, S. Shimomura, T. Wakahara, M. Tachibana, *J. Cryst. Growth*, **388**, 5–11 (2014).
25) H.-X. Ji, J.-S. Hu, Q.-X. Tang, W.-G. Song, C.-R. Wang, W.-P. Hu, L.-J. Wan, S.-T. Lee, *J. Phys. Chem. C*, **111**, 10498–10502 (2007).
26) M. Tachibana, K. Kobayashi, T. Uchida, K. Kojima, M. Tanimura, K. Miyazawa, *Chem. Phys. Lett.*, **374**, 279–285 (2003).
27) H. Takeya, K. Miyazawa, R. Kato, T. Wakahara, T. Ozaki, H. Okazaki, T. Yamaguchi, Y. Takano, *Molecules*, **17**, 4851–4859 (2012).
28) H. Takeya, R. Kato, T. Wakahara, K. Miyazawa, T. Yamaguchi, T. Ozaki, H. Okazaki, Y. Takano, *Mater. Res. Bull.*, **48**, 343–345 (2013).
29) K. Miyazawa, C. Hirata, T. Wakahara, *J. Cryst. Growth*, **405**, 68–72 (2014).
30) C. L. Ringor, K. Miyazawa, J. Nanosci. *Nanotechnol.*, **9**, 6560–6564 (2009).
31) 宮澤薫一編著, "Fullerene Nanowhiskers", Pan Stanford Publishing Pte. Ltd. (2011).

筆者紹介
宮澤　薫一　独立行政法人物質・材料研究機構先端材料プロセスユニット　フラーレン工学グループ　グループリーダー　工学博士

1985年東京大学大学院工学系研究科金属材料学専門課程博士課程退学，同年東京大学文部技官，1986年東京大学工学部助手，1989年東京大学講師，2002年㈱物質・材料研究機構主幹研究員，現在に至る．
連絡先　〒305-0044　茨城県つくば市並木1-1
（勤務先）

(2014. 11. 13受付)
(2014. 12. 1受理)

ENVIRONMENTAL TOXICOLOGY AND PHARMACOLOGY 39 (2015) 879–886

Available online at www.sciencedirect.com

ScienceDirect

journal homepage: www.elsevier.com/locate/etap

Titanium dioxide nanoparticles exacerbate pneumonia in respiratory syncytial virus (RSV)-infected mice

Seiko Hashiguchi [a], Hiroki Yoshida [b], Toshi Akashi [c], Keiji Komemoto [a], Tomoyuki Ueda [a], Yoshiaki Ikarashi [d], Aki Miyauchi [c], Katsuhiko Konno [b], Sayoko Yamanaka [b], Akihiko Hirose [e], Masahiko Kurokawa [b], Wataru Watanabe [a,*]

[a] Department of Microbiology, Graduate School of Clinical Pharmacy, Kyushu University of Health and Welfare, 1714-1 Yoshino, Nobeoka, Miyazaki 882-8508, Japan

[b] Department of Biochemistry, Graduate School of Clinical Pharmacy, Kyushu University of Health and Welfare, 1714-1 Yoshino, Nobeoka, Miyazaki 882-8508, Japan

[c] Department of Microbiology and Infectious Diseases, School of Pharmaceutical Sciences, Kyushu University of Health and Welfare, 1714-1 Yoshino, Nobeoka, Miyazaki 882-8508, Japan

[d] Division of Environmental Chemistry, National Institute of Health Sciences, 1-18-1 Kamiyoga, Setagaya-ku, Tokyo 158-8501, Japan

[e] Division of Risk Assessment, Biological Safety Research Center, National Institute of Health Sciences, 1-18-1 Kamiyoga, Setagaya-ku, Tokyo 158-8501, Japan

ARTICLE INFO

Article history:
Received 4 November 2014
Received in revised form 23 February 2015
Accepted 24 February 2015
Available online 3 March 2015

Keywords:
Titanium dioxide
Nanoparticles
Respiratory syncytial virus
Pneumonia

ABSTRACT

To reveal the effects of TiO_2 nanoparticles, used in cosmetics and building materials, on the immune response, a respiratory syncytial virus (RSV) infection mouse model was used. BALB/c mice were exposed once intranasally to TiO_2 at 0.5 mg/kg and infected intranasally with RSV five days later. The levels of IFN-γ and chemokine CCL5, representative markers of pneumonia, in the bronchoalveolar lavage fluids of RSV-infected mice had increased significantly in TiO_2-exposed mice compared with the control on day 5 post-infection, but not in uninfected mice. While pulmonary viral titers were not affected by TiO_2 exposure, an increase in the infiltration of lymphocytes into the alveolar septa in lung tissues was observed. Immunohistochemical analysis revealed aggregation of TiO_2 nanoparticles near inflammatory cells in the severely affected region. Thus, a single exposure to TiO_2 nanoparticles affected the immune system and exacerbated pneumonia in RSV-infected mice.

Abbreviations: TiO_2, titanium dioxide; RSV, respiratory syncytial virus; IFN-γ, interferon-gamma; BALF, bronchoalveolar lavage fluids; BFRs, brominated flame retardants; DBDE, decabrominated diphenyl ether; TBBPA, tetrabromobisphenol A; PBS, phosphate-buffered saline; IL, interleukin; PFU, plaque-forming units; ELISA, enzyme-linked immunosorbent assay; LPS, lipopolysaccharide.

* *Corresponding author*. Tel.: +81 982 23 5685; fax: +81 982 23 5685.
E-mail address: w_watal@phoenix.ac.jp (W. Watanabe).

http://dx.doi.org/10.1016/j.etap.2015.02.017
1382-6689/

1. Introduction

Nanomaterials are engineered structures with at least one dimension of 100 nm or less (Nel et al., 2006). Various kinds of nanomaterials are known and have a wide range of applications (Maidalawieh et al., 2014; Nel et al., 2006; Stamatoiu et al., 2012). Titanium dioxide (TiO_2) nanoparticles are used in cosmetics and building materials because they are chemically and thermally stable. When research focused on TiO_2 nanoparticles were in drug delivery systems (Zhang et al., 2012) several findings of toxicity due to exposure to TiO_2 nanoparticles were reported, such as carcinogenesis of the lung in rats (Xu et al., 2010), induction of strong oxidative stress and mitochondrial damage in glial cells (Huerta-Garcia et al., 2014), and inflammatory disorder on the cardiovascular system in ApoE knockout mice (Chen et al., 2013). Although we are exposed to TiO_2 nanoparticles in daily life, the safety of TiO_2 nanoparticles for human health is poorly known.

Human respiratory syncytial virus (RSV), a member of the *Paramyxoviridae* family, is a prevalent infectious agent of acute lower respiratory illness in infants and young children (MacDonald et al., 1982). An initial RSV infection is frequent during the first few years of life, and most children have been infected by 24 months of age (Collins et al., 2001). Clinically severe RSV infection is seen primarily in infants and young children with naïve immune systems and/or genetic predispositions (Holberg et al., 1991) and patients with suppressed T-cell immunity (MacDonald et al., 1982). RSV reinfects adults at a rate of approximately 5–10% per year (Falsey, 2007), and is an important cause of morbidity and mortality in the elderly (Falsey et al., 2005). Thus, because the severity of RSV infection reflects the condition of the host immunity, we established a novel assay system for evaluation of the immunotoxicity of the brominated flame retardants (BFRs) using a murine model of RSV infection (Watanabe et al., 2008a). We subsequently demonstrated that decabrominated diphenyl ether (DBDE) (Watanabe et al., 2008b, 2010a) and tetrabromobisphenol A (TBBPA) (Takeshita et al., 2013; Watanabe et al., 2010b) caused developmental immunotoxicity and irregular production of cytokines in RSV-infected mice, respectively. In addition, we also revealed that perinatal exposure to methamidophos, a representative organophosphate insecticide, suppressed the production of proinflammatory cytokines using this model (Watanabe et al., 2013).

In the present study, we adopted the RSV infection mouse model to evaluate the effects of TiO_2 nanoparticles on the immunotoxicity after a single exposure. Then we investigated the effects of TiO_2 nanoparticles on pneumonia in RSV infection by focusing on the variations in of cytokine and chemokine levels in bronchoalveolar lavage fluid (BALF) and the exacerbation of pneumonia in lung tissues by histopathological assay.

2. Materials and methods

2.1. *Animals*

Female (5 weeks old) BALB/c mice were purchased from Kyudo Animal Laboratory (Kumamoto, Japan) and housed at 25 ± 2 °C. The mice were allowed free access to the conventional solid diet CRF-1 (Oriental Yeast Co., Chiba, Japan) and water and used in this experiment after 7 d acclimation. The animal experimentation guideline of the Kyushu University of Health and Welfare were followed in the animal studies.

2.2. *Cell and virus*

The A2 strain of RSV was obtained from American Type Culture Collection (ATCC, Rockville, MD) and grown in HEp-2 cell (human epidermoid carcinoma, ATCC CCL-23) cultures. Viral titers of HEp-2 cells were measured by the plaque method (Watanabe et al., 2008a) and expressed as plaque-forming units per milliliter (PFU/mL).

2.3. *Chemical compound*

TiO_2 nanoparticles were kindly provided by Tayca Corp. (Osaka, Japan). The particles form ultra-fine rutile crystals primarily 35 nm in diameter. TiO_2 nanoparticles readily aggregate to form microparticles in phosphate-buffered saline (PBS). To avoid aggregation, the suspension of TiO_2 nanoparticles in PBS was dispersed using a portable ultrasonic disruptor just before treatment of mice. Then the mean secondary diameter of the particles was 913 nm, ranging from 804 to 1022 nm, as measured by a Zetasizer Nano (Malvern Instruments, Worcestershire, UK).

2.4. *Animal tests*

Six-week-old mice were intranasally administered 0.1 mL of a suspension of TiO_2 nanoparticles at 0.25 or 2.5 mg/kg of body weight one time under anesthesia for histological assays or 0.5 mg/kg for measuring cytokines in BALF and pulmonary viral titers. In control group, mice were given PBS intranasally under anesthesia.

The RSV infection test was performed as reported previously (Watanabe et al., 2008a). Briefly, 5 d after from TiO_2 exposure, mice were infected intranasally with 3.5×10^5 PFU of the A2 strain of RSV under anesthesia. In a mock-infected group, mice were given PBS intranasally. On day 5 after infection, blood samples were prepared from RSV-infected mice under anesthesia and BALF was obtained from the mice under anesthesia by instilling 0.8 mL of cold PBS into the lungs and aspirating it from the trachea using a tracheal cannula. Following the acquisition of BALF, the lungs were removed, immediately frozen in liquid N_2, and stored at −80 °C until virus titration. Ice-cold BALF was centrifuged at $160 \times g$ at 4 °C for 10 min. After centrifugation, the supernatant was stored at −80 °C until to use. The cell pellet was suspended in 0.3 mL of cellbanker-1 (Nippon Zenyaku Kogyo Co., Ltd., Koriyama, Japan) as bronchoalveolar lavage cells, and then stored at −80 °C prior to use. Frozen lung tissue was homogenized with cold quartz sand in a homogenizer. After centrifugation at $480 \times g$ at 4 °C for 15 min, the supernatants of the homogenates were used for a plaque assay. Viral titers in lungs of mice were expressed as PFU/mL.

2.5. ELISA

Interleukin (IL)-2, IL-4, IL-10, and interferon (IFN)-γ levels in BALF were measured using specific ELISA kits (Ready-set-go, eBioscience Inc., San Diego, CA) according to the manufacturer's instructions. Levels of CCL5 (RANTES) in BALF and serum and CCL3 (MIP-1α) in BALF and the culture supernatant of bronchoalveolar lavage cells were measured using specific ELISA kits (Quantikine, R&D Systems, Inc., Minneapolis, MN) according to the manufacturer's instructions. The lower limits of detection of the kits are 2 (pg/mL) for IL-2, 4 (pg/mL) for IL-4, 8 (pg/mL) for IL-10, 15 (pg/mL) for IFN-γ, 2 (pg/mL) for CCL5, and 1.5 (pg/mL) for CCL3. The intra- and interassay coefficients of variation for the ELISA results were less than 10%.

2.6. Flow cytometric analysis of bronchoalveolar lavage cells

Flow cytometric analysis was performed according to our previous report (Takeda et al., 2014). Briefly, bronchoalveolar lavage cells were stimulated with BD GolgiStop (BD PharMingen, San Diego, CA) at 1 μL/mL for 6 h at 37 °C. After incubation, the cells were washed twice and stained for intracellular IFN-γ (FITS Rat Anti-Mouse IFN-γ, BD PharMingen, San Diego) and IL-4 (PE Rat Anti-Mouse IFN-γ, BD PharMingen, San Diego), according to the manufacturer's instructions. The cells were washed twice and analyzed on an FACS Calibur 35 flow cytometer (Becton Dicknson, Sunnyvale, CA).

2.7. Histological methods and evaluation

For histological examination of RSV-infected lungs, 3–5 mice per group of infected mice were sacrificed by cervical dislocation on day 5 after infection, and the lungs were removed and placed in buffered formalin for a minimum of 24 h. The tissue was then embedded in low-melting point paraffin, sectioned at a thickness of 5 μm, and stained with hematoxylin and eosin. After taking two pictures randomly of each pulmonary lobe using a microscope (×100), the pictures were analyzed for the proportion of alveolar septa and infiltration of the inflammatory cells into the tissues per unit area by Adobe Photoshop (Adobe Systems, Inc., San Jose, CA).

2.8. Immunohistochemical evaluation

The lung tissue sections were deparaffinized and hydrated through xylenes and graded alcohols. After washing with water, they were incubated in unmasking solution (Vector Laboratories, Inc., Burlingame, CA) at 90 °C for 30 min. Then, the sections were incubated in the 0.3% H_2O_2 in PBS for 30 min to quench the endogenous peroxidase activity and treated with blocking serum (Vector Laboratories, Inc.) for 30 min. The lung tissues were stained with a goat polyclonal antibody against RSV protein (1:250, Acris Antibodies GmbH, Inc., San Diego, CA) for 90 min. Then, RSV proteins were detected using a VECTASTAIN ABC kit (Vector Laboratories, Inc.) according to the manufacturer's instructions. The sections were faintly counterstained with hematoxylin.

2.9. Culture of bronchoalveolar lavage cells

Culture of bronchoalveolar lavage cells obtained from RSV-infected mice on day 1 post-infection was performed according to our previous report (Watanabe et al., 2010a). Briefly, 200 μL of bronchoalveolar lavage cells suspension (2.5×10^5 cells/mL) was seeded on each well in a 96-well microtiter plate and incubated at 37 °C for 24 h in a humidified air with 5% CO_2. After incubation, the culture medium was removed by aspiration and replaced in fresh RPMI medium with or without 0.1 mg/mL of TiO_2 nanoparticles. Following 24 h further incubation, the culture medium was removed by aspiration and replaced in fresh RPMI medium with or without 100 ng/mL of lipopolysaccharide (W *E. coli* O127: B8, Difco, Detroit, MI; LPS) for 24 h. The culture supernatant was harvested from each well and the amount of CCL3 was measured by ELISA.

2.10. Statistical analysis

Comparisons between the pulmonary viral titers and the levels of cytokines and chemokines of the control and TiO_2-treated groups were carried out using Student's t-test. A P value of 0.05 or less was considered to be significant.

3. Results

3.1. Effects of TiO_2 nanoparticles on RSV infection in mice

To investigate the effects of TiO_2 nanoparticles on the immune response to RSV infection, six-week-old female BALB/c mice were exposed intranasally to 0.1 mL of TiO_2 suspension at 0.5 mg/kg of body weight under anesthesia. No abnormal behavior or dystrophy due to the stress of TiO_2 exposure was observed compared to the control (0 mg/kg) in the mice, and the mice were infected intranasally with the A2 strain of RSV at 3.5×10^5 PFU five days after TiO_2 exposure. The levels of IFN-γ, a representative marker of pneumonia in RSV infection, in BALF were measured on day 5 post-infection (Table 1). The IFN-γ levels of RSV-infected mice treated with TiO_2 were significantly ($P < 0.05$) higher than those in the control. In mock-infected mice treated with or without TiO_2, the levels of IFN-γ in BALF were under the limit of detection. These results indicated that pneumonia in RSV-infected mice was exacerbated by TiO_2 exposure. To investigate further effects of exposure to TiO_2 on the immune system of RSV-infected mice, the levels of Th1 cytokines (IFN-γ and IL-2) and Th2 cytokines (IL-4 and IL-10) in BALF were also measured on day 5 after infection (Table 1). The levels of IL-10 in BALF were significantly ($P < 0.05$) increased by approximately 92% compared with the control. No significant increase of IL-2 in BALF was found after TiO_2 treatment, and the levels of IL-4 in BALF were under the limit of detection. In mock-infected mice treated with or without TiO_2, the levels of cytokines in BALF were under the limit of detection. To reveal effects of exposure to TiO_2 on the Th1/2 immune balance of RSV-infected mice on day 5 post-infection, intracellular IFN-γ and IL-4 productions by the bronchoalveolar lavage cells were examined by flow cytometry (Table 2).

Table 1 – Effects of TiO_2 on levels of cytokines in BALF of RSV-infected mice on day 5 post-infection.

TiO_2 exposure (mg/kg)	Concentration (ng/mL)[a]							
	RSV-infected				Mock-infected			
	IFN-γ	IL-2	IL-4	IL-10	IFN-γ	IL-2	IL-4	IL-10
0	8.59 ± 3.44	0.02 ± 0.01	<0.01	1.65 ± 0.71	<0.01	<0.01	<0.01	<0.01
0.5	12.90 ± 2.10*	0.03 ± 0.01	<0.01	3.17 ± 1.15*	<0.01	<0.01	<0.01	<0.01

[a] Concentration (ng/mL) of each cytokine in BALF from RSV-infected mice treated with or without TiO_2 (0.5 mg/kg) was measured by ELISA for each specific cytokine. Data represents mean values of 3–6 mice. Numbers in parentheses indicate standard deviation.
* Statistically different from control at $P < 0.05$ (Student's t-test).

Table 2 – Effects of TiO_2 on intracellular cytokine levels in bronchoalveolar lavage cells on day 5 post-infection from RSV-infected mice.

TiO_2 exposure (mg/kg)	% of total population[a]			
	$IFN\text{-}\gamma^-IL\text{-}4^-$	$IFN\text{-}\gamma^+IL\text{-}4^-$	$IFN\text{-}\gamma^-IL\text{-}4^+$	$IFN\text{-}\gamma^+IL\text{-}4^+$
0	98.7	1.1	0.1	0.1
0.5	98.9	0.8	0.1	0.2

[a] Bronchoalveolar lavage cells were collected from RSV-infected mice treated with or without TiO_2 (0.5 mg/kg) on day 5 post-infection. The pooled bronchoalveolar lavage cells were stimulated BD GolgiStop for 6 h at 37 °C and stained intracellular IFN-γ and IL-4. The stained cells were analyzed by flow cytometry.

There was not a significant change in the population of IFN-γ-positive cells and IL-4-positive cells due to TiO_2 treatment. These results suggested that TiO_2 exposure should affect the immune response to RSV infection.

Chemokine CCL5 is a common marker of the severity of inflammation in the lungs due to RSV infection (Lambert et al., 2003) and chemokine CCL3 also is an inflammatory marker. Therefore, we measured the levels of CCL5 and CCL3 in BALF on day 5 after infection (Table 3). The levels of CCL5 in BALF were significantly ($P < 0.05$) increased by approximately 36% compared with the control, but there was no significant increase of CCL3 levels in TiO_2-exposed mice. In mock-infected mice treated with or without TiO_2, the levels of chemokines in BALF were under the limit of detection. The levels of CCL5 in serum were significantly ($P < 0.05$) increased by approximately 31% compared with the control (Table 3). Thus, these results strongly suggested that TiO_2 exposure exacerbated the pneumonia due to RSV infection.

To evaluate the effects of TiO_2 exposure on the growth of RSV in mice, pulmonary viral titers were measured by plaque assay (Fig. 1). Viral titers of mice exposed to TiO_2 were not elevated significantly compared with those of control. Thus, TiO_2 exposure did not enhance proliferation of RSV in mice.

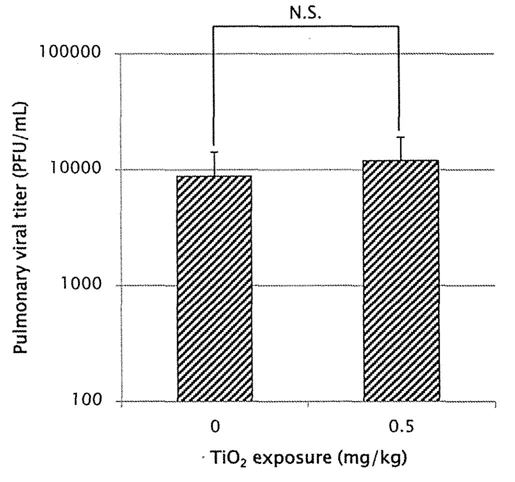

Fig. 1 – Effect of exposure to TiO_2 on pulmonary viral titers of RSV-infected mice on day 5 post-infection. The data represents mean ± standard deviation of values of 7 control or 5 TiO_2-treated mice. N.S., not significant.

3.2. *Effects of TiO_2 nanoparticles on severity of pneumonia in RSV infection*

To clarify the effects of TiO_2 nanoparticles on the severity of pneumonia in RSV infection, a histopathological assay was performed. In this experiment, 3–5 mice in each group were treated with TiO_2 as follows: a control group at 0 mg/kg, low-dose group at 0.25 mg/kg, and high-dose group at 2.5 mg/kg. These mice were infected with or without RSV 5 days after TiO_2 exposure. On day 5 post-infection, the mice were sacrificed, and their lung tissues were analyzed histopathologically. Representative results and changes in severity are presented in Fig. 2 and Table 4, respectively. In mock-infected mice, no obvious change in the lung tissues due to TiO_2 exposure was observed compared with the control (Fig. 2A-a, -c, and -e). In RSV-infected mice, typical features of pneumonia due to RSV infection, such as degeneration of the bronchial epithelium and infiltration of lymphocytes and neutrophils, were observed in mice treated with or without TiO_2 (Fig. 2A-b, -d, and -f). Severity of pneumonia was assessed as the proportion of alveolar septum tissue in RSV-infected mice (Table 4). In the control group at 0 mg/kg, the proportion of alveolar septa of all mice was less than 60%. On the other hand, two mice in the TiO_2 (0.25 mg/kg)-treated group had more than 60% alveolar septa, and one mouse in the TiO_2 (2.5 mg/kg)-treated group had more than 70%. The unit area means were 51.8%, 60.6%,